Modeling Activities Related to Waste Form Degradation: Progress Report

Fuel Cycle Research & Development

Prepared for
U.S. Department of Energy
Spent Fuel Waste Science and Technology

Carlos F. Jové Colón,
Harry Moffat,
Philippe Weck,
Louise Criscenti,
Mekalah Padilla,
David Sassani

Sandia National Laboratories
June 30, 2022

SAND22-XXXX

Sandia National Laboratories is a multimission laboratory managed and operated by National Technology and Engineering Solutions of Sandia, LLC, a wholly owned subsidiary of Honeywell International, Inc., for the U.S. Department of Energy's National Nuclear Security Administration under contract DE-NA-0003525.

This page is intentionally blank.

AKNOWLEDGEMENTS

The authors acknowledge our gratitude to Prasad Nair (DOE NE-81) and Tim Gunter (DOE NE-81) for their helpful discussions and contributions on various topics covered in this report. This work was supported by the DOE-NE SFWD office.

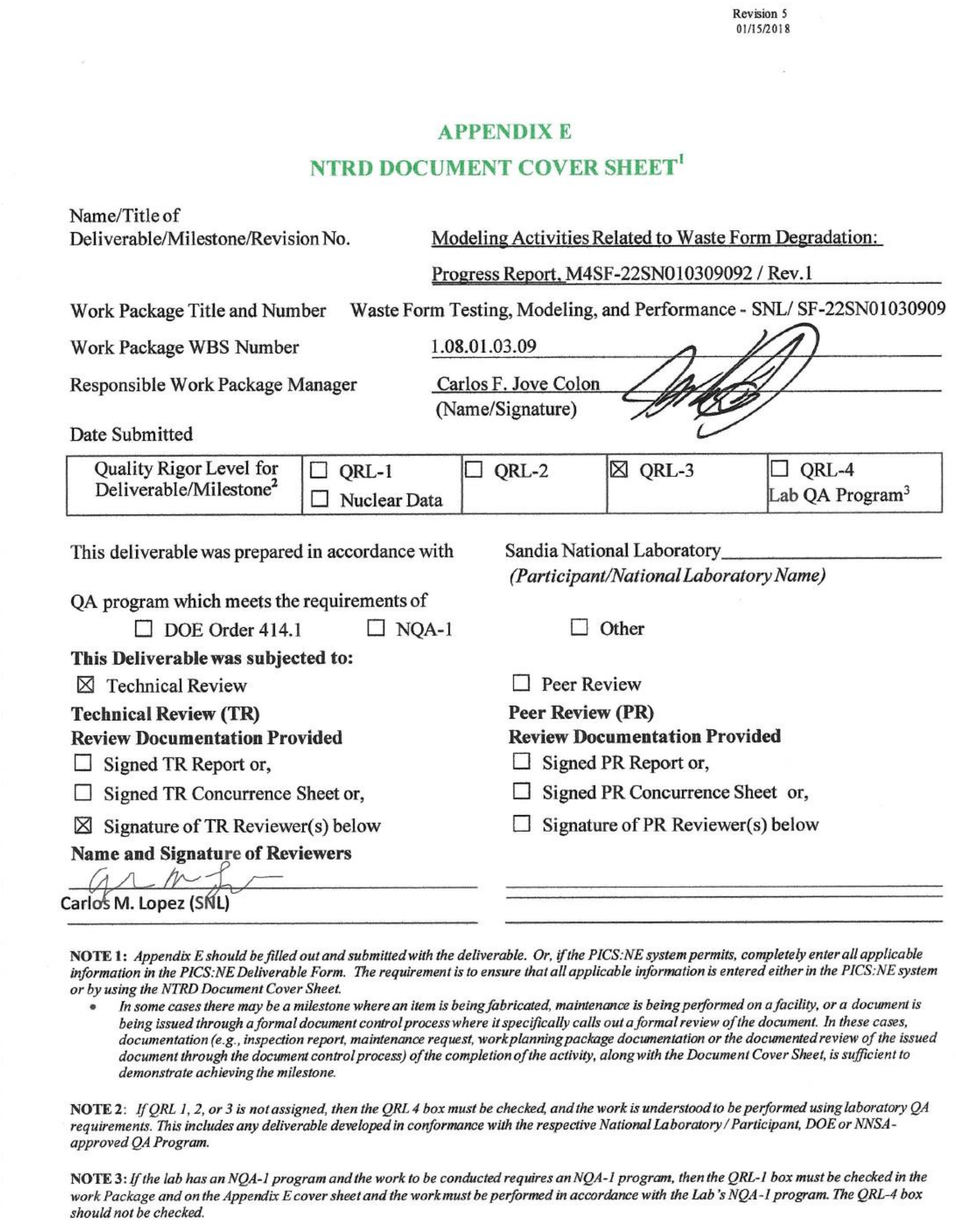

Revision 5
01/15/2018

APPENDIX E
NTRD DOCUMENT COVER SHEET[1]

Name/Title of Deliverable/Milestone/Revision No. Modeling Activities Related to Waste Form Degradation: Progress Report, M4SF-22SN010309092 / Rev.1

Work Package Title and Number Waste Form Testing, Modeling, and Performance - SNL/ SF-22SN01030909

Work Package WBS Number 1.08.01.03.09

Responsible Work Package Manager Carlos F. Jove Colon
(Name/Signature)

Date Submitted

Quality Rigor Level for Deliverable/Milestone[2]	☐ QRL-1 ☐ Nuclear Data	☐ QRL-2	☒ QRL-3	☐ QRL-4 Lab QA Program[3]

This deliverable was prepared in accordance with Sandia National Laboratory
(Participant/National Laboratory Name)

QA program which meets the requirements of

☐ DOE Order 414.1 ☐ NQA-1 ☐ Other

This Deliverable was subjected to:

☒ Technical Review ☐ Peer Review

Technical Review (TR) **Review Documentation Provided**	**Peer Review (PR)** **Review Documentation Provided**
☐ Signed TR Report or,	☐ Signed PR Report or,
☐ Signed TR Concurrence Sheet or,	☐ Signed PR Concurrence Sheet or,
☒ Signature of TR Reviewer(s) below	☐ Signature of PR Reviewer(s) below

Name and Signature of Reviewers

Carlos M. Lopez (SNL)

NOTE 1: *Appendix E should be filled out and submitted with the deliverable. Or, if the PICS:NE system permits, completely enter all applicable information in the PICS:NE Deliverable Form. The requirement is to ensure that all applicable information is entered either in the PICS:NE system or by using the NTRD Document Cover Sheet.*

- *In some cases there may be a milestone where an item is being fabricated, maintenance is being performed on a facility, or a document is being issued through a formal document control process where it specifically calls out a formal review of the document. In these cases, documentation (e.g., inspection report, maintenance request, work planning package documentation or the documented review of the issued document through the document control process) of the completion of the activity, along with the Document Cover Sheet, is sufficient to demonstrate achieving the milestone.*

NOTE 2: *If QRL 1, 2, or 3 is not assigned, then the QRL 4 box must be checked, and the work is understood to be performed using laboratory QA requirements. This includes any deliverable developed in conformance with the respective National Laboratory / Participant, DOE or NNSA-approved QA Program.*

NOTE 3: *If the lab has an NQA-1 program and the work to be conducted requires an NQA-1 program, then the QRL-1 box must be checked in the work Package and on the Appendix E cover sheet and the work must be performed in accordance with the Lab's NQA-1 program. The QRL-4 box should not be checked.*

This page is intentionally blank

Table of Contents

Table of Figures

REVISION HISTORY

M4SF-21SN010309021	Rev.2

Acronym List

ALTGLASS	Accelerated Leach Testing Glass
ANL	Argonne National Laboratory
ASTM	American Society for Testing Materials
DAE	differential algebraic equation
DFT	Density Functional Theory (
DFPT	density functional perturbation theory
DOE	Department of Energy
DOE-NE	DOE Office of Nuclear Energy
DSNF	DOE-managed spent nuclear fuel
EBS	Engineered Barrier System
EDS	Energy Dispersive Spectroscopy
EDZ	Excavated Disturbed Zone
EELS	Electron Energy-Loss Spectroscopy
GDSA	geologic disposal safety analyses
GDSA PA	Geological Disposal Safety Analyses Performance Assessment
GRAAL	Glass Reactivity with Allowance for the Alteration Layer
HLW	high-level radioactive waste
HSTFs	Hanford Site Tank Farms
ICP-OES	Inductively Coupled Plasma Optical Emission Spectroscopy
ICP-MS	Inductively Coupled Plasma Mass Spectrometry
IRF	Instant Relief Fraction
ISG	International Simple Glass
IWM	integrated waste management
JAEA	Japan Atomic Energy Agency
MAS	Magic Angle Spin
MRWFD	Materials Recovery and Waste Form Development
NEA	Nuclear Energy Agency
NIST	National Institures of Standards and Technology
NMR	Nuclear Magnetic Resonance
NS	Natural System
ORNL	Oak Ridge National Laboratory
OWL	Online Waste Library

PA	performance assessment
PBE	Perdew, Burke, and Ernzerhof
PNNL	Pacific Northwest National Laboratory
PRI	passivating reactive interphase
PWR	pressurized water reactor
QHA	quasiharmonic approximation
R&D	research and development
R&D	Research & Development
SF	Spent Fuel
SFWD	Spent Fuel and Waste Disposition
SFWST	Spent Fuel and Waste Science and Technology
SHE	Standard Hydrogen Electrode
SI	Saturation Indices
SIMFUEL	Simulated (spent) Fuel
S&T	Storage and Transportation
SNF	Spent Nuclear Fuel
SNL	Sandia National Laboratories
SRSTF	Savannah River Site Tank Farms
STEM-HAADF	Scanning Transmission Electron Microscopy with High-Angle Annular Dark-Field detector
TEM(EFTEM)	Transmission Electron Microscopy (Energy Filtered Transmission Electron Microscopy)
TST	Transition State Theory
US DOE	United States Department of Energy
VASP	Vienna Ab initio Simulation Package
XRD	X-ray Diffraction
XRF	X-ray Fluorescence

I. Introduction

This report represents the milestone deliverable M4SF-22SN010309092 “Modeling Activities Related to Waste Form Degradation: Progress Report” that describes the progress of R&D activities of ongoing modeling investigations specifically on nuclear waste glass degradation, Density Functional Theory (DFT) studies on clarkeite structure and stability, and electrochemical model development of spent nuclear fuel (SNF). These activities are part of the Waste Form Testing, Modeling, and Performance work package at Sandia National Laboratories (SNL). This work package is part of the “Inventory and Waste Form Characteristics and Performance” control account that includes various experimental and modeling activities on nuclear waste degradation conducted at Oak Ridge National Laboratory (ORNL), SNL, Argonne National Laboratory (ANL), and Pacific Northwest National Laboratory (PNNL).

ORNL developed an experimental test plan for the evaluation of commercial SNF degradation under conditions relevant to deep geological nuclear waste repository environments. The integration of all these multi-laboratory R&D activities are illustrated in Fig. 1. These include experimental/modeling work on SNF SIMFUEL (ANL), cladding degradation (SNL/PNNL), high-resolution isotopic studies (ORNL), development of the Online Waste Library (OWL; SNL), chemical characterization studies using the SALVI microfluidic cell (PNNL), and aqueous actinide speciation at elevated temperatures(LANL). It is expected that integrations of these activities will also intersect research work conducted in the storage and transportation (S&T) campaign, integrated waste management (IWM), and other SFWD R&D efforts. Many of the experimental/modeling investigations in Fig. 1 are ongoing while others are being planned as proposed work. Details of the ongoing investigations depicted in Fig. 1 will also be described in in milestone deliverable reports from their respective laboratory research groups.

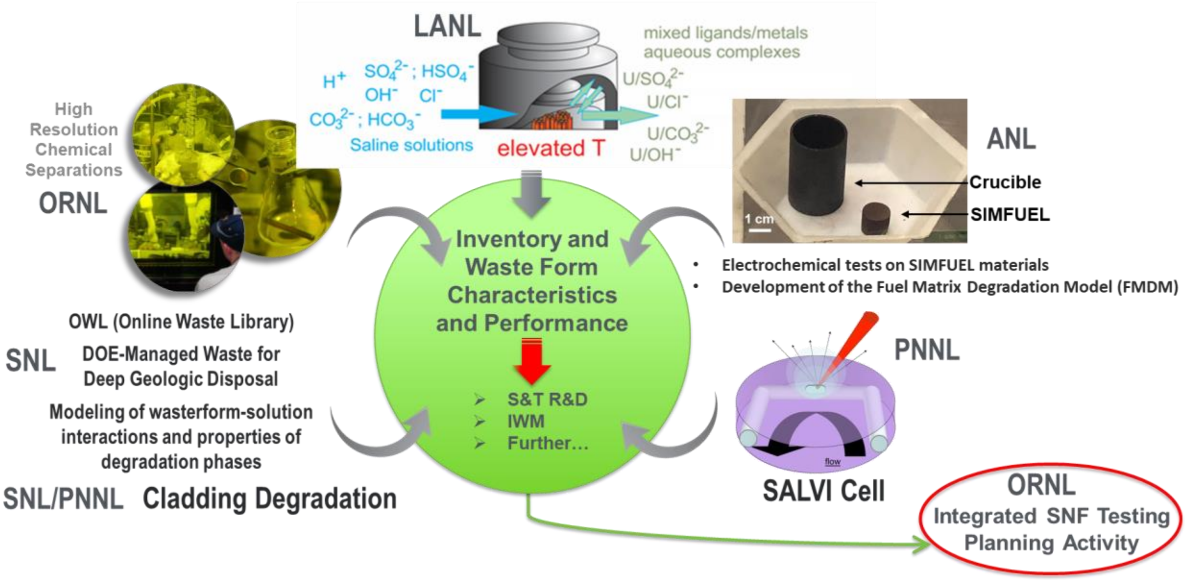

Figure 1. Schematic diagram illustrating the integration of multi-laboratory experimental and modeling research activities in the study of waste form degradation and source-term characteristics (adapted from Jové Colón and Sassani, 2021). Contributions to this figure kindly provided by personnel from each laboratory research group.

It is envisioned that this planning will result in a program that entails the development and integration of experimental and modeling activities to improve the representation of the source term fuel degradation models in investigations supporting the safety assessment and the Geologic Disposal Safety Analyses (GDSA) Performance Assessment (PA). Fig. 2 shows the relational structure of source term processes in the GDSA (Mariner et al., 2019). The main processes considered in the GDSA PA are waste package degradation, SNF cladding degradation, instant release fraction (IRF), and SNF dissolution. The SNF testing plan by ORNL in the report "Draft Gap Analysis and Strategy for Commercial Spent Nuclear Fuel Degradation in Generic Repository Environments: Focus on Fuel Matrix Degradation" (M3SF-22OR010309032; Meszaros et al. 2022)describes various aspects of proposed experimental activities to evaluate these processes and their prioritization in R&D activities. The report outlines the prioritization methodology based on the combined gap priority and methodology readiness scores.

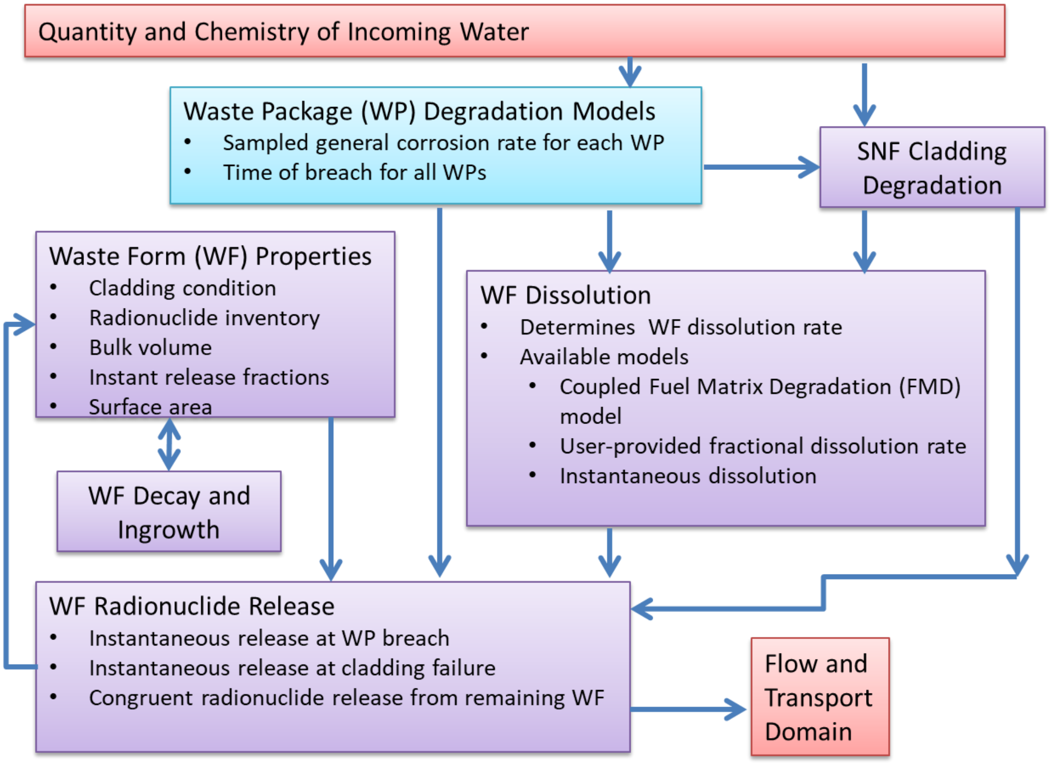

Figure 2. Conceptual Framework for Source Term Processes in GDSA (Adapted from Mariner, et al., 2019)

Potential waste forms considered in GDSA PA efforts and the constrains on their degradation rates have been evaluated for waste form types in various disposal concepts (e.g., Sassani et al. 2017). The waste forms considered in that report include (1) SNF, (2) HLW glass (and other glass waste), and (3) DSNF HIP calcine waste. Weck et al. (2021) provides of summary of literature with emphasis on stage III waste glass degradation model being developed external to the SFWST Campaign. In this report, the continuation of this glass degradation work is presented with the use of a zeolite thermodynamic database (zeo19; Zhen-Wu et al. 2020) and its application in reaction path modeling to evaluate the resumptive Stage III in glass degradation rate. This report also evaluates the structural and stability properties of clarkeite polymorphs based on density functional theory (DFT) calculations. The development of a zero-D multiphase multicomponent electrochemical model for UO_2 is also described. The objective of this model is to provide a more robust evaluation of the electrochemical degradation behavior of SNF degradation based on the thermodynamic properties of all phases.

It is anticipated that these modeling activities will support the assessments of wasteform degradation in conjunction with experimental/testing efforts to represent in-package chemistry, and source term processes in GDSA-PA.

II. Waste Glass Degradation

Weck et al. (2021) and Jové Colón et al. (2021) provides a summary of key R&D literature on waste glass degradation. For the sake of completeness, the main aspects of that literature summary will be repeated here and to some extent expanded if necessary. Several reports (Criscenti and Sassani 2010; Freeze et al. 2011; Criscenti et al. 2011) summarize research on waste glass degradation rates using models and experiments to study three major stages (Vienna et al. 2018):

1. The initial far-from-equilibrium (glass-solution) rates, or Stage I rates, in which the fresh glass surface reacts with solution and the glass dissolution rate is high;
2. Evolution to slower, longer term Stage II rates, in which alteration layers (e.g., diffusion layer, gel layer, secondary phase layer) are forming on glass surfaces and growing at different rates relative to one another, allowing the solution at the glass interface to approach equilibrium resulting in a degradation rate approaching steady state;
3. At the later stages of the experiment, glass degradation rates increase dramatically with the onset of Stage III, which is characterized by a resurgence in glass dissolution accompanied by the precipitation of more stable secondary phases.

Understanding the accelerated or resumptive dissolution rate behavior (Stage III) of glass after exhibiting steady-state or residual for a prolonged period time is key to long-term waste glass degradation. Recent international efforts have focused on investigating glass degradation rates in more detail to improve our understanding of the transition to increased Stage III rates under uncertain conditions during the Stage II (slower, or *residual*) rate behavior of HLW glasses (Fig. 3). The objective is to develop a mechanistic understanding of the transition to higher dissolution rates such that glass degradation models can account explicitly for these changes and the detailed behavior can be incorporated into PA models.

The solution chemistry of nuclear waste glass degradation evolves naturally towards alkaline conditions. However, because some systems may remain far from pH conditions set by the HLW glass itself a mechanistic analysis of this process leads to the development of a comprehensive rate law over the full range of pH values. Strachan (2017) evaluated the form of dissolution rate equations (e.g., Pierce et al. 2008; Cassingham et al. 2015) used for glass dissolution that accounts for Stage I dissolution under acidic, neutral, and alkaline conditions. Strachan (2017) refitted the basalt glass dissolution rate data of Gislason and Oelkers (2003) with a two-term, acid-based version of this rate law. The two-term rate law in Strachan (2017) provides a good representation of the experimental data for basalt glass dissolution without a term involving Al^{3+}.

$$rate_G = k_0 \times 10^{\eta \cdot pH} \times \left[\exp\left(\frac{-E_a}{RT} \right) \right] \times \left[1 - \frac{Q}{K} \right] + k_{long}$$

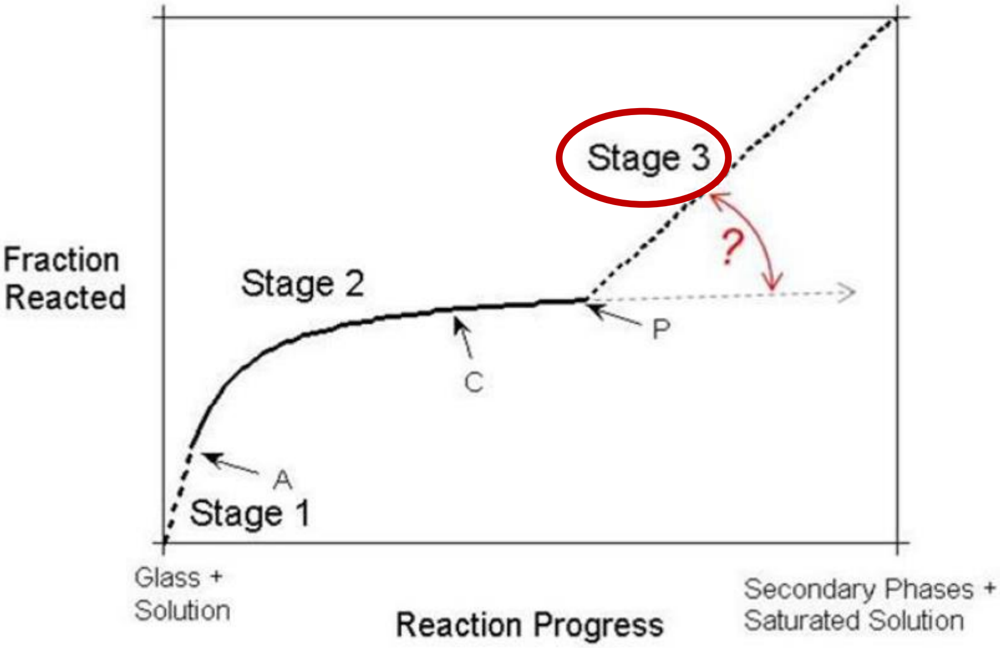

Source: Modified from Ebert 2017.

Figure 3. HLW glass rate law with pH dependency along with schematic plot showing the temporal evolution of glass dissolution (after Ebert and Jantzen, 2017a).

Frugier et al. (2008) show that as glass dissolves, a gel layer is formed between the pristine glass and the aqueous solution. The importance of this gel layer in terms of its role in glass degradation remains a topic of research. Porous media diffusion of glass constituents out through the gel into aqueous solution and of dissolved species from the solution to the pristine glass surface is suggested. This diffusive process may become the rate-limiting mechanism as the solution at the glass surface becomes closer to being dominated by the glass constituents. Secondary phases nucleate and precipitate within the gel layer suggesting that the trigger for Stage III degradation rates is in this layer (Fournier et al. 2014). Research focusing on the trigger for Stage III evaluates (1) the pristine glass composition, (2) the gel composition, and/or (3) the conditions of degradation including temperature and solution pH (Frugier et al. 2008, 2009).

Strachan and Croak (2000) performed geochemical calculations to evaluate the formation of analcime in static glass dissolution experiment. The experiments indicated that analcime formation leads to an increase in dissolution rate for certain glasses, however, such behavior was not observed in other types of glasses. These calculations, which were performed using the EQ3/6 software package (Wolery and Jarek, 2003), only allowed four phases to precipitate: analcime, amorphous silica, gibbsite, and calcite. A simple glass defined by six constituents — SiO_2, Al_2O_3, B_2O_3, Na_2O, CaO, and Li_2O — was considered in this study. The calculations were performed assuming that H_4SiO_4 is the dominant dissolved Si species. It is suggested that analcime precipitation will decrease silica saturation, thereby increasing glass dissolution in Stage III. The results of this study suggest that analcime precipitation has a strong dependence on the Al content of the glass. For glass with ratios of Si/(Si+Al) < 0.7, the amount of glass that must dissolve is only 1/100 to 1/1,000 of that for glasses with higher ratios before analcime precipitation triggers Stage III rates. Strachan and Neeway (2014) calculated the relationship between glass dissolution rates and the precipitation of analcime and concluded that, in the absence of a gel layer, the rate of glass dissolution and the rate of analcime precipitation are coupled. Like Strachan and Croak (2000), Strachan and Neeway (2014) also noted that analcime formed most readily from glasses that had higher Al content.

Jantzen et al. (2017a,b) created a glass corrosion database (ALTGLASS^{TM}) that has been used to determine if gel compositions which evolve are correlated with the generation of zeolites and increased (Stage III) glass dissolution rates. Using the database, the study team estimated gel compositions based on the difference between the elemental glass starting compositions and the measured elemental leachate concentrations for glasses that had been leached for 15–20 years. The results demonstrated that hydrogel compositions with Si*/Al* ratios of <1.0 (Si* and Al* are defined as the activated Si and Al in the gel) did not generate zeolites and maintained low dissolution rates for the duration of the experiments. These hydrogels have an overall stoichiometry of allophane-hisingerite ($(Al,Fe)_2O_3 \bullet 1.3\text{-}2Si(OH)_4$) and precipitate clay minerals. Glasses that formed hydrogel compositions with Si*/Al* ratios >1 precipitated zeolites and were accompanied by a resumption in the glass dissolution rate. These hydrogels have a stoichiometry close to that of imogolite ($Al_2O_3 \bullet Si(OH)_4$) with ferrihydrite ($Fe_2O_3 \bullet 0.5H_2O$). Interaction of these hydrogels with excess alkali from the glass and OH^- in the leachates causes the formation of zeolites. In summary, according to this study, the critical factors required for zeolite formation are a hydrogel Si*/Al* ratio >1 and a pH >10. It is also suggested that the high pH values of the leachate solutions are directly proportional to the alkali content of the glass.

Gin et al. (2015) conducted experiments on the International Simple Glass (ISG) at 90^{o}C in a solution initially saturated with respect to amorphous $^{29}SiO_2$ (i.e., ~Stage 2 conditions). At pH 9, the corrosion rate continuously drops, and the glass slowly transforms into a uniform, homogenous, amorphous alteration layer. At pH 11.5, the alteration process changes where the glass completely dissolves and secondary phases precipitate. At pH 11.5, the glass dissolution rate is maintained close to that in Stage I by the hydrolysis of the silicate network promoted by OH^- and by the precipitation of zeolites and other less stable phases. Fournier et al. (2017) followed this work by introducing zeolite seeds into the ISG leaching experiments. They concluded that high pH values combined with high Al concentrations in solution lead to zeolite precipitation, and that the sudden decrease in Al concentrations caused by zeolite formation leads to an increase in glass dissolution rate. In agreement with Gin et al. (2015), the study results demonstrated that the effect of zeolite precipitation decreases with decreasing pH and temperature and was no longer detectable in unseeded leaching experiments conducted at pH 9. These experiments show that the glass composition alone is insufficient to determine if the transition to Stage III will occur and that different pH conditions can lead to different long-term outcomes. Crum et al. (2021) evaluated Stage III behavior for a waste glass experimental matrix having a wide compositional coverage using zeolite-seeded glass dissolution experiments.

Fournier et al. (2018) further investigated the effect of zeolite precipitation on the dissolution kinetics of the ISG using the GRAAL (Glass Reactivity with Allowance for the Alteration Layer) model. The GRAAL model relies on the reactivity (i.e., formation and dissolution) of a transport-limiting layer called the passivating reactive interphase (PRI) (Frugier et al. 2008, 2018).

The equations used in the GRAAL model by Fournier et al. (2018) to study ISG dissolution include expressions for (1) zeolite nucleation and growth, (2) first-order rate laws to constrain the Si/Al and Ca/Al ratios of the gel layer to the stoichiometry $SiAl_{0.3}Ca_{0.15}O_{2.6}$, and (3) first-order rate laws derived from transition state theory (TST) to describe the precipitation of secondary phases including both zeolites and C-S-H. Fournier et al. (2018) argue that to match experiments, the Si/Al ratio of the PRI should be in the 0.1–0.7 range. They also point out that using the solubility of the endmember $SiAl_{0.3}Ca_{0.15}O_{2.6}$ in the rate expression accounts for the roles of Al and Ca on Si precipitation at pH > 10.

Gin (1995) first suggested that Al is involved in the rate-limiting reaction and defined a mixed Al-Si activity product, but McGrail et al. (1997, 2001) found this proposed ion activity product to be inconsistent with the existing data and modeling of glass dissolution. Others have also proposed a role of Al^{3+} in the rate-limiting reaction (Bourcier 1994; Hamilton et al. 2000; Abraitis et al. 2000; Hamilton et al. 2001; Oelkers and Gislason 2001; McGrail et al. 2001; Gislason and Oelkers 2003; Criscenti et al. 2005, 2006). The rate laws of Oelkers and Gislason (2001) and Gislason and Oelkers (2003) suggest that at constant [H_4SiO_4], the rates should increase with decreasing Al^{3+}.

Because the gel layer between the glass and the aqueous solution appears to play a key role in nuclear waste glass dissolution, many researchers have focused on understanding this gel layer in detail. One of the key issues under investigation is whether the gel layer is (1) a residual glass layer formed by the incongruent dissolution of the glass (i.e., preferential leaching of mobile cations leaving behind the framework glass structure), or (2) the result of congruent dissolution of the glass followed by precipitation of an amorphous silica-rich layer. Another issue under debate is the role of the gel layer in glass degradation. Does the gel layer passivate the glass surface slowing glass dissolution because now glass and aqueous solution components must diffuse through this protective layer, or does the gel layer enhance glass degradation by providing nucleation sites for secondary minerals, or both?

Hellmann et al. (2015) and Putnis (2015) both focus on how advanced atomic-resolution analytical techniques show that the structural and chemical interface between pristine glass and the altered zone is always extremely sharp, with gradients in the nanometer to subnanometer range. This observation supports the hypothesis that the alteration layer is a consequence of congruent dissolution followed by precipitation of an amorphous silica layer. The techniques used to observe this sharp interface include scanning transmission electron microscopy with a high-angle annular dark-field detector (STEM-HAADF), energy-filtered TEM (EFTEM) mapping, electron energy-loss spectroscopy (EELS), and atom probe tomography (Hellmann et al. 2015). Putnis (2015) points out that these results are consistent with experimental results that found that stable isotope tracers introduced in the aqueous solution (e.g., Geisler et al. 2010; Dohmen et al. 2013) were discovered in the alteration layer. Geisler et al. (2015) continued to conduct experiments using oxygen and silicon isotope tracers to study the degradation of ternary Na-borosilicate glasses and concluded that the experimental data fit with a model of congruent dissolution of the glass followed by the precipitation and growth of an amorphous silica layer. Geisler et al. (2019) conducted real-time *in-situ* experiments of reaction and transport phenomena during silicate glass corrosion by fluid-cell Raman spectroscopy. The formation of a water-rich zone (several micrometers thick) between the alteration/gel layers and the glass was found. This zone was detected, as were pH gradients at the glass surface and within the alteration layers. Using a deuterated solution, the researchers observed that water transport through the gel is not rate limiting. Ryan et al. (2019) conducted (Na-P2 zeolite) seeded and unseeded glass dissolution experiments of Na-aluminoborosilicate glass to study State III degradation behavior using in situ Raman spectroscopy. Their experiments showed the formation of analcime, suggesting that its stable precipitation may be impactful in glass dissolution.

Murphy et al. (2013) conducted experiments on both Advanced Fuel Cycle Initiative glass and a simplified version of this glass in ASTM type I water at 90°C and then used a suite of nuclear magnetic resonance (NMR) techniques to investigate the composition of the gel layer. Both glasses developed alteration layers composed primarily of Si species. Aluminum was also retained in the alteration layers, with a change in coordination from $^{[IV]}$Al to $^{[VI]}$Al, which correlates with a loss of charge-balancing cations. ^{1}H-^{11}B cross polarized magic angle spinning NMR observations indicated a retention of boron in the hydrated glass layer (defined as between the bulk glass and gel/alteration layer), a result that has not been characterized by previous work. The ratio of $^{[III]}$B/$^{[IV]}$B was found to be ~0.95 in the pristine glass. Secondary phases in the alteration layers (termed precursor phases) were identified as crystalline sodium metasilicates.

Pierce et al. (2010) studied the dissolution kinetics of five glasses along the $NaAlSiO_4$-$NaBSiO_4$ compositional join to evaluate how the structural variations related to the boron-aluminum substitution influence the glass dissolution rate. Analysis of unreacted glass samples by ^{27}Al and ^{29}Si magic angle spin (MAS) NMR suggested that most Al and Si atoms occupy a tetrahedral coordination, whereas B-atoms occupy both tetrahedral and trigonal coordination. The $^{[III]}$B is fractionated between $^{[III]}$B(ring) and $^{[IV]}$B(nonring) moieties with the $^{[III]}$B(ring)/$^{[III]}$B(nonring) ratio increasing with an increase in B/Al ratio. The fraction of $^{[IV]}$B also increases with B/Al ratio, and there appears to be mixing between the $^{[IV]}$Al and $^{[III]}$B sites, assuming avoidance between tetrahedral trivalent cations.

Within the Materials Recovery and Waste Form Development (MRWFD) Campaign within DOE-NE, the mechanistic behavior that initiates Stage III degradation rates for glass is being incorporated into a performance assessment model. When this MRWFD glass model becomes available, SFWST will incorporate this into GDSA so it can be used to represent glass long-term degradation behavior. This approach involves ongoing cross-campaign integration activities.

Discussion and Results

Additional Evaluations Conducted in FY2021-2022

To investigate how glass and leachate compositions influence the onset of Stage III in glass dissolution, we chose to look at the data sets for glass dissolution experiments reported in Jantzen et al. (2017a; Table 1). Those data include five glasses that exhibit Stage III dissolution (increased rates after the steady-state rates of Stage II) and four glasses that stayed at steady state rates. The data reported in Jantzen et al. (2017a) are supplemented by more detailed information in the ALTGLASS^{TM} database as well as data compiled for numerous other glasses. The experiments reported are batch leaching tests conducted at 90°C and 1 atm pressure. The glass compositions reported in both sources contain over 25 components, though for simplicity we are evaluating an idealized subset of the major constituents. Initial analyses of dissolved waste glass with time assumed that boron leached from the glass goes into solution (i.e., behaves conservatively) and does not become incorporated into either the secondary silica gel or in other secondary phases. Then, the calculated ratio using the mass of boron in solution over the mass of boron in the initial glass was used as a proxy for the evolution of glass degradation. In the current analysis, reaction path modeling is used to evaluate the trends of major glass components with time. Using boron mass loss changes with time has been used as an indicator of glass dissolution (Ryan et al., 2019).

Modeling Approach to Evaluate Stage III Glass Dissolution

Past efforts have used the geochemistry code PHREEQC (Parkhurst, 1995) to calculate the aqueous speciation of each leachate composition and mineral saturation indices (SI) in these leachates. The calculations are performed assuming the solutions are in equilibrium with atmospheric pCO_2 at 90°C. This approach leads to a drop in pH values from the measured pH determined at 25°C. As expected, at higher pH the dominant silica species in solution transitions from $Si(OH)_4$ to $HSiO_3^-$ and the dominant alumina complex is $Al(OH)_4^-$. Several mineral SIs are being computed including kaolinite, (Ca, Na, H)-nontronite, analcime, (Ca, Na, H)-beidellite, phillipsite, quartz, and boehmite, to evaluate what stable solid phases may be supersaturated in the fluids. Though not entirely clear mechanistically, it appears that the transition to Stage III (higher) degradation rates may be directly affected by precipitation of stable phases in the experiments, such as zeolite phases. Investigating the chemical changes to the solution along its reaction path (where the solution evolves from far-from equilibrium with respect to the glass composition, to something that is more controlled by the glass composition) may provide insights to potential phase changes that could drive the system to a higher rate of degradation in Stage III.

During glass degradation, a metastable gel layer is formed from the reaction of the unstable glass with the solution. The Stage III degradation may be triggered by more stable phase(s) precipitating within or near the gel layer (Bourcier et al., 1989; Strachan and Croak, 2000; Strachan, 2001; Fournier et al., 2014; Ebert and Jantzen, 2017a,b). It is the goal of the reaction path simulation to provide a relatively simplistic zero-D representation of the glass dissolution process mainly based on mass transfer relations between solids and solution, capturing the system feedbacks imposed by dissolution kinetics of the glass reactant and secondary mineral equilibria in the evolving solution chemistry. This is particularly important for controls on dissolved Si in the system by the formation of zeolite phases and to identify the key compositional variables of the leachates that lead to Stage III rate initiation.

Toward this objective, reaction path modeling has been performed using the computer code EQ3/6 (Wolery and Jarek, 2003) with an updated thermodynamic database to include a suite of zeolites from the zeo19 database (Zhen-Wu et al., 2020) and clay phases (nontronite, saponite, kaolinite). Thermodynamic data for the for nontronite and saponite phases is based on the work by Gailhanou et al. (2013). Updated thermodynamic data for kaolinite is from Blanc et al. (2015). Hereon, the analcime-2.5 model results will be the focus of the current study given the wide occurrence and association of analcime during Stage III glass degradation. The transition state theory (TST) rate law expression in EQ3/6 was used by only considering the dependence on the activity of $SiO_2(aq)$ for the degradation of the glass phase. Strachan (2017) evaluated some of the TST kinetic models applied to glass dissolution. Gin et al. (2008) discusses the application of kinetic rate laws and the limitations of such with chemical affinity terms when applied to (boro)silicate glass dissolution. In the current study, the conditions for glass dissolution are far from equilibrium and under such the TST-based rate law is used to essentially evaluate the dependencies on the activity of $SiO_2(aq)$ on glass dissolution with the formation of secondary phases.

The additional glass phases selected for this work whose leaching behavior is considered resumptive for this modeling exercise are the West Valley waste glasses after Jantzen et al.

(2017a; Table 1 therein): WVUTh198, WVUTh122, and WVCM59. The main reason for selecting these three (out of five) is because of their similar leaching behavior in temporal changes of major glass components such as dissolved Si and Na. These similarities allow for useful comparisons and rate parameter evaluation between different glass dissolution data sets. The other two glasses (WVUTh203 and AFCI) have resumptive leaching behavior but their temporal solute concentration trends are rather different from the other three glasses.

Jantzen et al. (2017a) also tabulate glasses with steady-state residual leaching for which only one (WVUTh179) was evaluated in this work. The compositions of West Valley glasses and alteration phases have been described by Ribet et al. (2004), Muller et al. (2006), and Jantzen et al. (2017a). It should be noted that some of the West Valley glasses bulk Fe_2O_3 content can be up to ~12 weight percent. The observed secondary phases in the dissolution studies for this glass are nontronite and zeolite (phillipsite) according to the ALTGLASS^{TM} glass corrosion database (Jantzen et al., 2017a).

Jové Colón et al. (2021) examined the resumptive behavior of the WVUTh198 glass whose dissolution behavior is similar to WVUTh122 and WVCM59. Figure 4 shows reaction path modeling results from Jové Colón et al. (2021) depicting the total Si concentration vs. time for two cases assuming a zeolite alteration solid: analcime-2.5 and Na-phillipsite. Both cases yielded very similar results, with some differences at early times but nearly identical at later times. The model assumes partial equilibrium where secondary minerals precipitate instantaneously in the reaction path, therefore, no kinetics are specified for the alteration phases (Ebert and Jantzen, 2017b). The reaction path modeling approach assuming analcime-2.5 as the zeolite and kaolinite as the clay as the main secondary Al-silicate phases used to evaluate WVUTh198 glass dissolution is also adopted for these two glasses as well.

For the EQ3/6 reaction path simulations, the following phases were considered for either inclusion/suppression in the evaluation of glass dissolution behavior: analcime ($Na_{0.85}Al_{0.85}Si_{2.15}O_6 \bullet H_2O$ or analcime-2.5), nontronite NAu-1 ($Ca_{0.247}K_{0.020}Si_{3.458}Al_{0.818}Mg_{0.068}Fe_{1.688}O_{10}(OH)_2$), Na-phillipsite ($NaAlSi_3O_8 \bullet 3H2O$), brucite ($Mg(OH)_2$), chalcedony ($SiO_2$), and kaolinite ($Al_2Si_2O_5(OH)_4$). Goethite (FeOOH) was also considered in certain cases for comparisons with dissolved Fe experimental data. The nontronite NAu-1 thermodynamic data given by Gailhanou et al. (2013) is for a Ca-saturated composition. Chalcedony is used in the model as a proxy for an amorphous silica-rich phase. The inclusion of either analcime or Na-phillipsite were considered separately to evaluate the effect of the zeolite type in the resulting temporal evolution of solute concentration profiles. Although analcime was not reported as a secondary phase in the WVUTh198 glass degradation experiment, it has been observed in other West Valley glass degradation studies showing resumptive behavior.

For the reaction modeling approach in this work, it is assumed that analcime is part of the secondary mineral assemblage in all glasses showing resumptive behavior. The EQ3/6 code runs were conducted in a closed system model at a temperature of 90°C (1 bar) for consistency with experiments. The initial reacting solution is a very diluted water with total carbonate of 10^{-3} molal. An arbitrary logK value of 50 was assigned to the dissolution reaction of the WVUTh198 glass. The constant surface area specified for the glass is 1900 cm^2. The objective for using a large positive logK value is to "destabilize" the glass dissociation reaction into its products and effectively maintain far from equilibrium conditions. Linard et al. (2001a,b) studied the thermochemistry of nuclear waste glasses and estimated a positive logK value for Na-borosilicate glass.

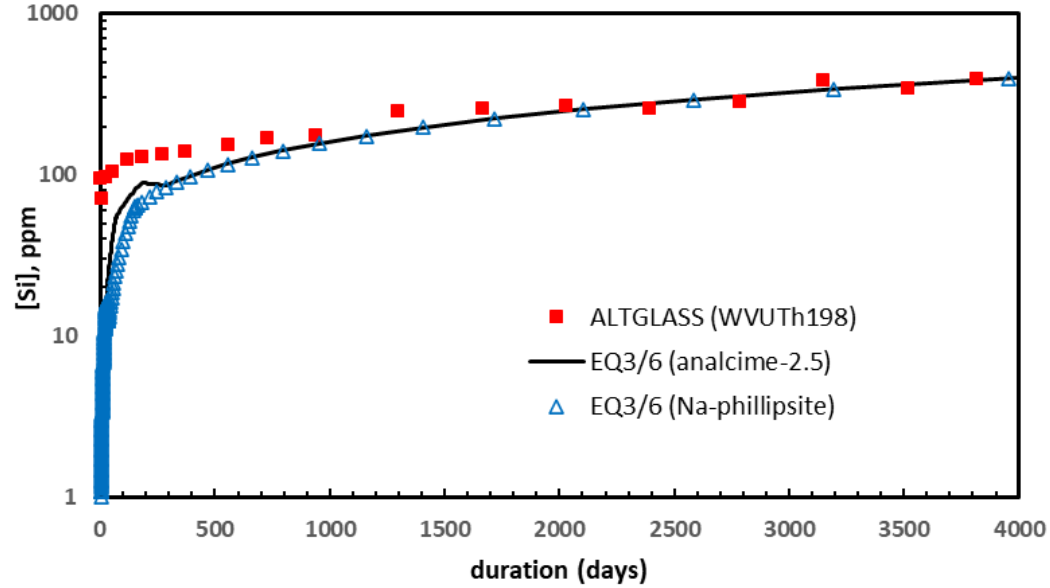

Figure 4. Semi-log plot of the EQ3/6 reaction path results (solid line) and experimental total Si concentration data (symbols) for the WVUTh198 glass dissolution (Jové Colón et al., 2021). The fits to the experimental data are given for the cases were either analcime-2.5 and Na-phillipsite are assumed to be the controlling zeolite solid phase. WVUTh198 glass dissolution data from the ALTGLASSTM glass corrosion database (Jantzen et al., 2017a).

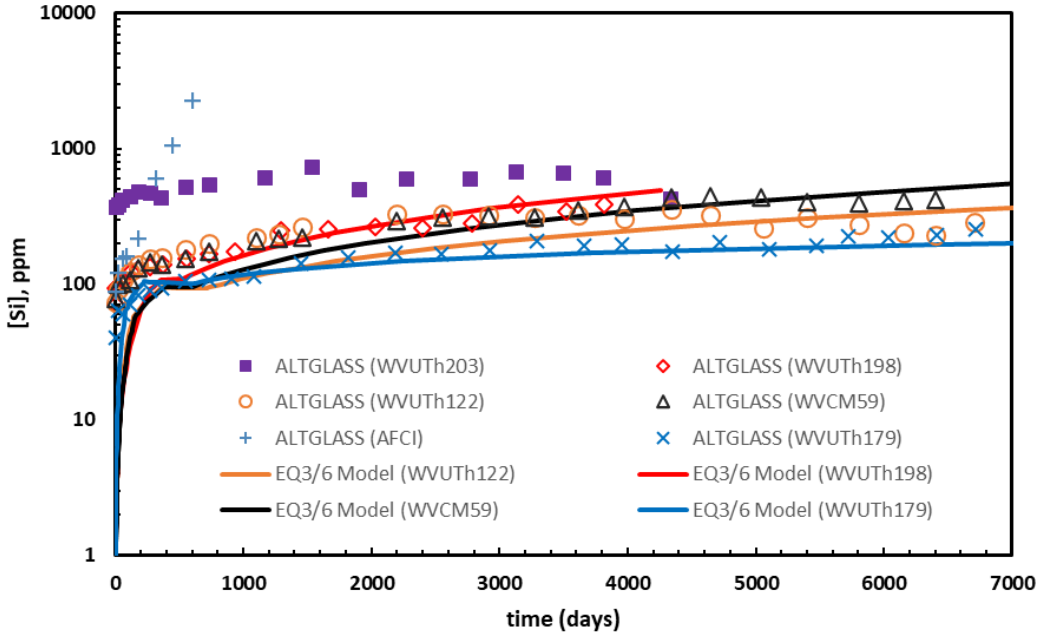

Figure 5. Semi-log plot of the EQ3/6 reaction path results (solid lines) and experimental total Si concentration data (symbols) for the considered glasses from the ALTGLASSTM glass corrosion database (Jantzen et al., 2017a). The AFCI and WVUTh203 glasses were not modeled in this study.

Fig. 5 shows the experimental data and EQ6 reaction path modeling results as total Si concentration vs. time for additional glasses showing resumptive dissolution behavior (Jantzen et al. 2017a). As can be see seen in the plot, the model curves for glasses with resumptive behavior underpredict the experimental data at early times but with better agreement at later times. The spread of model curves at later times provides a good representation of the data spread even within the limits of the data. It should be noted that the WVUTh179 glass is listed in Jantzen et al. (2017a) as having a non-resumptive (or residual steady state) dissolution behavior. However, the model results for this glass presented in Fig. 5 considered the presence of analcime zeolite in the reaction path simulation. Also note that the total Si concentration in the temporal profile is the lowest among the considered data set. Although the model fit is in good agreement with the total Si concentration data of the WVUTh179 glass, the model fit to other solutes such as Na, Li, and B are overpredicted, suggesting a closer look to the considered model choices for rate parameters and secondary mineral phase assemblage. Fitting the experimental total Si concentration data without the formation of zeolite was attempted but only resulted in close representation at later times. Fig. 6 shows the predicted total Na concentration profiles with time showing a general correspondence with experimental data at later times. However, discrepancies in predicted Na concentrations tend to be larger, particularly in the case of the WVUTh179 glass which is regarded as having a non-resumptive dissolution behavior.

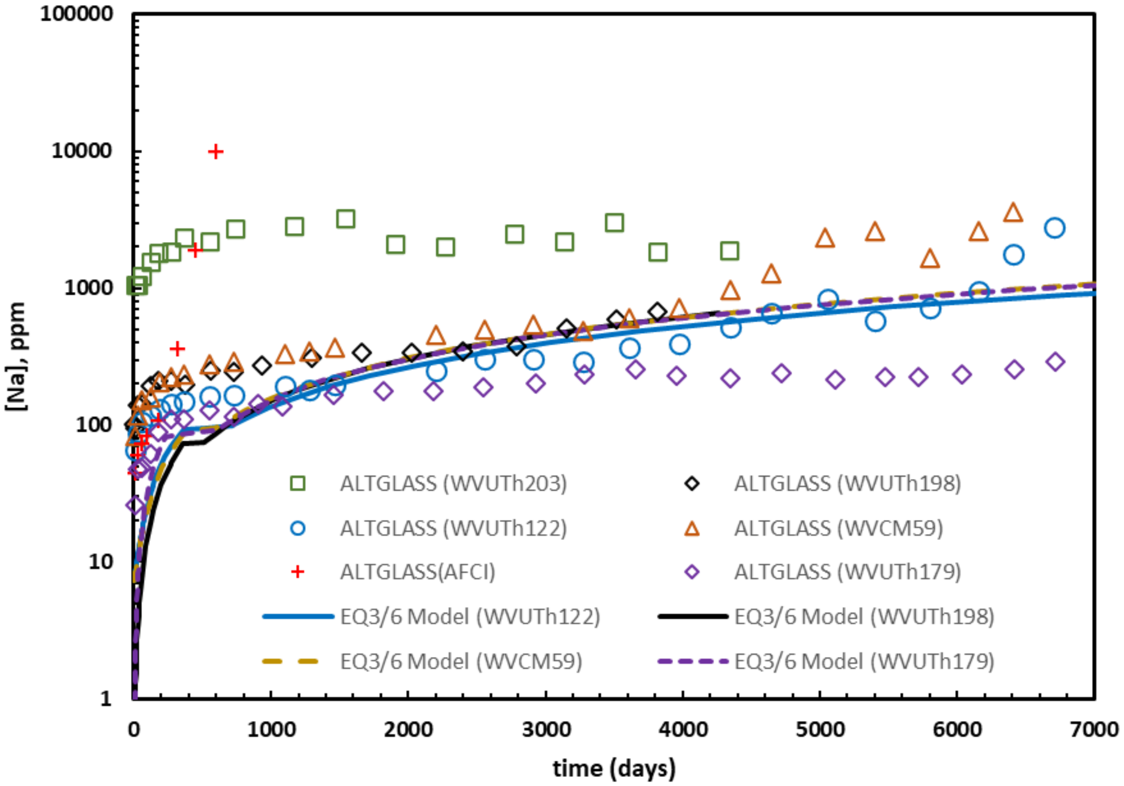

Figure 6. Semi-log plot of the EQ3/6 reaction path results (solid lines) and experimental total Na concentration data (symbols) for the considered glasses from the ALTGLASSTM glass corrosion database (Jantzen et al., 2017a). The AFCI and WVUTh203 glasses were not modeled in this study. The modeled curves for the WVUTh198, WVCM59, and WVUTh179 overlap at times over ~626 days.

The overall EQ3/6 reaction path model results show the following features apply for all the considered glasses with resumptive dissolution behavior:

- Kaolinite (and nontronite when included as part of the phase assemblage) saturate early in the reaction path (see Figs. 5a,b). The nontronite clay phase has Ca as a component and its concentration was not reported in the solution chemistry as part of the ALTGLASS ™ database. Therefore, its appearance in the model is poorly constrained and kaolinite is then treated as a proxy for a phyllosilicate alteration phase.
- The model predicts a pH increase very similar to the trend given by the experimental data (not shown). The attained pH values (computed at 90°C) at late times for most code runs ranged from pH~10 to pH~10.6. The lowest computed pH~9.3 was for the WVUTh179 glass.
- Chalcedony and analcime-2.5 precipitates at later times causing changes in the predicted Si concentration and mass of product solids vs. time profiles (Figs. 7a,b; WVUTh1198 glass).
- Upon analcime-2.5 saturation, the total Si concentration vs. time trend resembles that of a residual or steady-state behavior, approximating that referred as Stage II in glass dissolution.
- The exhaustion or consumption of kaolinite in the systems triggers the onset of an increase in dissolved Si which is concomitant with the continuous increases in analcime and chalcedony masses. Such increase in total Si concentration resembles a Stage III resumption or increase in glass dissolution at later times (Fig. 7b; WVUTh1198 glass).
- The computed Na and B concentrations are somewhat underpredicted at early times but with reasonable differences at later times. As noted previously, the concentrations of these solutes are overpredicted for the WVUTh179 glass.

Table 1 provides a list of the apparent rate constants and the exponent value of the $SiO_2(aq)$ activity term for the TST rate law expression as implemented in EQ3/6 for each of the modeled glasses. These values were adjusted to produce the closest fit to the experimental total Si concentration vs. time profile of the considered glasses; mainly constrained on Si releases at later times. Notice that the exponent for the $SiO_{2(aq)}$ activity is fixed to the same value of 0.24 for all glasses. The values for the logarithm of the apparent rate constant (k) used in glasses with resumptive dissolution behavior are all in good agreement. This could explain the overall close similarity in the total silica vs. time profiles for these glasses. However, there are still some discrepancies with the predicted concentrations of other components like Na, B, and Li.

Table 1. TST rate law parameters used in the dissolution of the considered waste glasses.

ALTGLASS Type	Activity Product Species	Product Species Exponent	Log Apparent Rate Constant (k) ($mol/cm^2/sec$)	Remarks
WVCM59	$SiO_2(aq)$	0.24	-12.07	Resumptive behavior
WVUTh179	$SiO_2(aq)$	0.24	-11.70	Steady state
WVUTh122	$SiO_2(aq)$	0.24	-12.00	Resumptive behavior
WVUTh198	$SiO_2(aq)$	0.24	-12.10	Resumptive behavior

Similar to the observations reported in Jové Colón et al. (2021), discrepancies in model predictions for the considered glasses significantly improve after ~600 days. This also includes the prediction of a resumptive Stage III dissolution trend based on the effect of secondary phase formation. This is particularly relevant to the formation of analcime zeolite and a Si-rich phase (represented in the model by chalcedony) as secondary phases exerting control on the increased glass dissolution rate in Stage III. Even when these results are still preliminary, the use of a relatively simplistic reaction path modeling with updated thermodynamic data for zeolites and clay provides a testing base for the role of these solids in reproducing Stage III behavior during glass degradation.

More work is needed to further test reaction path dependencies on included and suppressed mineral phases, in particular the role of secondary clay on Si release at early times and its relative stability throughout the simulation time with pH increases. Also of interest is assessing the effects of Fe-bearing phases like goethite (FeOOH) along with nontronite as secondary phases. This would also include sensitivities to clay phase saturation on the observed temporal profiles along with zeolite formation plus the effect on predicted pH.

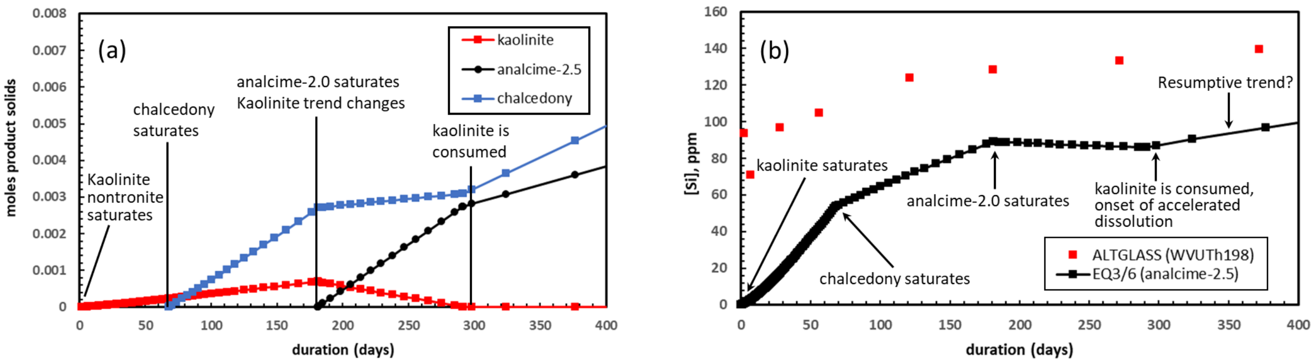

Figure 7. Plot of EQ3/6 reaction path results up to 400 days to show key changes in the WVUTh198 glass dissolution trends: (a) mass transfer plot of moles of product solids. Vertical lines delineate times corresponding to the addition/removal of key secondary phases. (b) Evolution of total Si concentration with time showing the effect of addition/removal of key secondary phases on the concentration profile. Notice the increase in Si concentration after 300 days coinciding with kaolinite removal which may be indicative of a resumptive trend in Stage III glass degradation. WVUTh198 glass dissolution data from the ALTGLASSTM glass corrosion database (Jantzen et al., 2017a).

III. Structures and Thermodynamics of Crystalline Clarkeite: Density Functional Theory (DFT) Study on Sodium Uranate Stability

Thermodynamic parameters for the corrosion phases of spent nuclear fuel (SNF), engineered barrier systems (EBS) materials and natural system (NS) minerals are critical to assess their stability and behavior in geologic disposal environments for safety assessments. The thermal properties of NS minerals surrounding the waste package (e.g., clays, complex salts, granite…) are of particular importance to determine phase stability of materials and interfacial processes leading to the degradation of the waste package. Jové Colón et al. (2021) provided descriptions of existing structural data and DFT calculations sodium uranate stability and their polymorphs. The current work provides an update of the DFT calculations and retrieval of thermodynamic parameters with comparisons to existing experimental data.

Accurate knowledge of the structure, thermodynamics, and phase stability relations of secondary corrosion phases formed during degradation of spent nuclear fuel (SNF) is crucial to evaluate (post-closure) source term behavior and thence the fate of radionuclides in deep geological disposal environments. Thermal properties of mineral phases surrounding the waste package are of central importance in determining phase stability of materials and interfacial processes leading to the degradation of the waste package. While actinide solubilities under typical environmental conditions have been extensively studied and are overall well constrained, very limited data exist on uranium secondary phase structures, formation, and stability under alkaline conditions. Extreme alkaline conditions typically exist in nuclear waste storage in tank farms. King et al. (2010) showed that the primary crystalline phases of uranium observed in equilibrium with the tank waste supernatant solutions was the mineral clarkeite, with chemical formula of $Na[(UO_2)O(OH)]\cdot(H_2O)_{0\text{-}1}$ (Finch and Ewing, 1997). This observation of the mineral clarkeite or sodium diuranate at the Savannah River Site Tank Farms (SRSTFs) is consistent with predictions that both phases should be the predominant uranium solid phases formed under alkaline conditions (Giammar, 2004).

Alkaline sludge and alkaline supernatant liquid wastes from REDOX and PUREX processes have been stored at the Hanford Site Tank Farms (HSTFs) (Carlstorm, 1977) and, similarly to nuclear waste storage at the SRSTFs, the mineral clarkeite or sodium diuranate might be expected to form under such highly alkaline conditions. It should be noted as well that naturally-occurring clarkeite is associated with the alteration of pegmatitic uraninite (UO_2) under hydrothermal conditions (Finch and Ewing, 1997). The potential for SNF waste form interactions with predominantly Na-bearing groundwaters in long-term deep geological disposal could produce suitable chemical conditions for phases in the Na-U-O system to form.

To avoid inadvertent precipitation, crystallization, and accumulation of uranium phases in process vessels and transfer pipes at nuclear waste storage tank farms and also as a potential phase in SNF alteration, a comprehensive understanding of the complex relationships between crystal structures and thermodynamic stability in the sodium uranate system is necessary. However, as mentioned in previous studies, there has not been a clear consensus on the structures and relative thermal stabilities of the various phases in the Na-U-O system, in particular for $Na_2U_2O_7$ polymorphs (Gasperin, 1986; Ijdo, Akerboom, and Bontenbal, 2015).

In this study, first-principles methods are utilized to provide an independent assessment of existing experimental structural and thermodynamic data and possibly resolve contradictions in existing data in the Na-U-O system. This investigation is aimed at predicting missing thermodynamic data needed for understanding the complex relationships between crystal structures and thermodynamic stability of $Na_2U_2O_7$ polymorphs, as a fast, systematic, and early way to avoid using expensive and time-consuming real materials and to complement experiments. Specifically, as a continuation of FY21 modeling activities related to waste form degradation (Jové Colón et al., 2021), additional density functional theory (DFT) and density functional perturbation theory (DFPT) calculations were conducted to predict volume-dependent phonon properties, Gibbs free energies and isobaric heat capacities of the α-, β-, and γ-$Na_2U_2O_7$ polymorphs for direct comparison with calorimetric data. In depth structural analysis and systematic experiment-theory comparison have also been conducted during FY22. Details of our computational approach are provided in the next section, followed by a complete analysis and discussion of our results, with extensive comparison with experimental data.

The main objectives of the present study using first-principles methods are to:

- Calculate missing thermodynamic data needed for understanding the complex relationships between crystal structures and thermodynamic stability in the sodium uranate system, as a fast, systematic, and early way to avoid using expensive and time-consuming real materials and to complement experiments.
- Provide an independent assessment of existing experimental thermodynamic data and resolve contradictions in existing calorimetric data.
- Validate our computational approach using high-quality calorimetric data.

To assess our first-principles computational approach, structural optimization of α-, β-, and γ-$Na_2U_2O_7$ were carried out using density functional theory (DFT), followed by density functional perturbation theory (DFPT) calculations to determine their phonon and thermal properties. Details of our computational approach are given in the next section, followed by a complete analysis and discussion of our results.

Computational Methods

Structural relaxation of α-, β-, and γ-$Na_2U_2O_7$ polymorphs was done at 0 K with DFT implemented in the Vienna Ab initio Simulation Package (VASP) (Kresse and Furthmüller, 1996). Details of geometry optimization calculations were reported in previous studies (see, e.g., Jové Colón; Weck et al., 2012). The generalized gradient approximation (GGA) (Perdew et al., 1992), with the parameterization of Perdew, Burke, and Ernzerhof (PBE) (Perdew et al., 1996) was utilized to compute the exchange-correlation energy.

For each of the α-, β-, and γ-$Na_2U_2O_7$ $Na_2U_2O_7$ polymorphs, crystal structure optimization was carried out using standard DFT, followed by phonon frequency calculations using DFPT for the equilibrium structure as well as several expanded and compressed states in the vicinity of the equilibrium crystal structure to investigate thermal effects. Analysis from a set of phonon calculations in the vicinity of the computed equilibrium crystal structure was carried out to obtain thermal properties at constant pressure (e.g., the Gibbs free energy and the isobaric heat capacity) within a quasi-harmonic approximation (QHA). The QHA mentioned here introduces a volume dependence of phonon frequencies as a part of anharmonic effect (Togo et al., 2008).

The Gibbs free energy is defined at a constant pressure by the transformation:

$$G(T,P) = \min_V\left[U(V) + F_{phonon}(T;V) + PV\right],$$

where $\min_V$ [function of *V*] corresponds to a unique minimum of the expression between brackets with respect to the volume V, $U(V)$ is the total energy of the system, and P is the pressure. $U(V)$ and $F_{phonon}(T;V)$ were calculated and the thermodynamic functions of the right-hand sides of the equation above were fitted to the integral forms of the Vinet equation of state (EOS). The phonon contribution to the Helmholtz free energy at constant volume *V*, was calculated using the following formula:

$$F_{phonon}(T) = \frac{1}{2}\sum_{\mathbf{q},v}\hbar\omega_{\mathbf{q},v} + k_B T\sum_{\mathbf{q},v}\ln\left[1 - e^{-\beta\hbar\omega_{\mathbf{q},v}}\right],$$

where $\mathbf{q}$ and v are the wave vector and band index, $\hbar$ is the reduced Planck constant, $\hbar\omega_{\mathbf{q},v}$ is the energy of a single phonon with angular frequency $\omega_{\mathbf{q},v}$, k_B is the Boltzmann constant, T is the temperature of the system, and $\beta = (k_\mathrm{B}T)^{-1}$. The isobaric heat capacity versus temperature was also derived from the Gibbs free energy according to:

$$C_P(T,P) = -T\frac{\partial^2 G(T,P)}{\partial T^2}.$$

Results and Discussion

Structures of α-, β-, and γ-$Na_2U_2O_7$ polymorphs

The structures and relative stabilities of $Na_2U_2O_7$ polymorphs have been the topic of several experimental studies. Powder samples of $Na_2U_2O_7$ were first characterized as an isotypic lacunar structure of $CaUO_4$, crystallizing in the rhombohedral space group R-3m (IT No. 166, Z = 3/2) (Kovba et al., 1958), then hexagonal (Carnall et al., 1966), and monoclinic (Cordfunke and Loopstra, 1971). The structural information on $Na_2U_2O_7$ known up to 1974 was reviewed by Keller (Keller, 1975). Using a mixture of U_3O_8 and Na_2CO_3, Gasperin synthesized pure, single crystal γ-$Na_2U_2O_7$ polymorph at 1200 °C, which was found after cooling to adopt the space group R-3m with lattice parameters of a = 3.911(3) Å and c = 17.857(5) Å (Gasperin, 1986). Similar to γ-$Na_2U_2O_7$, the mineral clarkeite, $Na[(UO_2)O(OH)]\cdot(H_2O)_{0\text{-}1}$, was also characterized as crystalizing in the hexagonal R-3m space group (IT No. 166, Z = 3), with lattice parameters of a = 3.954(4) Å and c = 17.73(l) Å (Finch and Ewing, 1997). Using powder X-ray diffraction (XRD) data, Kovba (Kovba, 1972) found that the room temperature α-$Na_2U_2O_7$ structure adopts the $C2/m$ (IT No. 12) space group, with lattice parameters of a = 12.796(10), b =7.822(2), c = 6.896(4), and β = 111.42(6)°. Based on XRD measurements, Smith and coworkers (Smith et al., 2014) later found that the room-temperature α-$Na_2U_2O_7$ structure adopts the monoclinic space group $P2_1$, (IT No. 4, Z = 2) with lattice parameters a = 6.887(3) Å, b = 7.844(3) Å, c = 6.380(3) Å and β = 111.29(5)°, and is isostructural with $Na_2Np_2O_7$ and $K_2U_2O_7$ (Saine, 1989; Smith et al., 2011). Recently, the lower-temperature crystal structures of synthetic α- and β-$Na_2U_2O_7$ polymorphs were determined from neutron powder diffraction by Ijdo et al. (2015). At 293 K, α-$Na_2U_2O_7$ crystallizes in a monoclinic unit cell, space group $P2_1/a$ (IT No. 14, Z = 4), with a = 12.7617(14) Å, b =7.8384(10) Å, c = 6.8962(9) Å, β = 111.285(9)°. At 773K, β-$Na_2U_2O_7$ is also monoclinic, with space group C2/m (IT No. 12, Z = 4), and lattice parameters a = 12.933(1) Å, b = 7.887(1) Å, c = 6.9086(8) Å, and β = 110.816(10)°. Ijdo et al. suggested that the C2/m symmetry erroneous assignment by Kovba (1972) for the room-temperature phase of $Na_2U_2O_7$ might be the result of insufficient annealing, and consequently the possible occurrence of micro-twinning, in the room-temperature sample characterized with XRD by Kovba. This suggestion appears plausible owing to the slow kinetics of the α-$Na_2U_2O_7$ ⇔ β-$Na_2U_2O_7$ reversible transformation (Cordfunke et al., 1982; Ijdo et al., 2015).

The thermodynamic properties of $Na_2U_2O_7$ were studied experimentally by Cordfunke et al., along with polymorphism and reversible structural phase transitions at 638 K (α-$Na_2U_2O_7$ → β-$Na_2U_2O_7$) and 1348 K (β-$Na_2U_2O_7$ → γ-$Na_2U_2O_7$) (Cordfunke and Loopstra, 1971; Cordfunke et al., 1982). In light of the findings by Ijdo et al. (2015), Smith and coworkers (Smith et al., 2015) reinvestigated polymorphism for $Na_2U_2O_7$ and confirmed with XRD the existence of α-, β- and γ- $Na_2U_2O_7$, with α → β and β → γ phase transitions at above ~600 K and in the range 1223-1323 K, respectively. However, after complete cooling to room temperature of what they expected to be either pure β-$Na_2U_2O_7$ or γ-$Na_2U_2O_7$, the final XRD pattern always corresponded to a mixture of α and β phases. Therefore, a clear understanding of the relationships between structures and relative thermodynamic stabilities of the $Na_2U_2O_7$ polymorphs is still missing.

Structures of $Na_2U_2O_7$ polymorphs: Comparison between DFT and experiments

Structural parameters obtained in this study for the α-, β-, and γ-$Na_2U_2O_7$ crystal unit cells relaxed at the GGA/PBE level of theory are summarized in Table 2, along with values obtained from X-ray and neutron diffraction crystallographic studies (Gasperin, 1986; Smith et al., 2014; Smith et al., 2015; Ijdo et al., 2015) and recent DFT predictions (Smith et al., 2017).

Table 2. Structural parameters of α-, β-, and γ-$Na_2U_2O_7$ unit cells.[a]

Phase	α	α	β	γ
Symmetry	$P2_1/a$	$P2_1$	$C2/m$	$R\text{-}3m$
IT No.	14	4	12	166
Z	4	2	4	3
a(Å)	**13.024**	**6.909**	**13.022**	**3.989**
	12.7617[b]	6.887[c]	12.933[b]	3.911[d]
	12.778[e]		12.946[e]	3.987[e]
	13.1322[f]		13.125[f]	
b(Å)	**7.850**	**7.877**	**7.850**	**7.964**
	7.8384[b]	7.844[c]	7.887[b]	7.822[d]
	7.823[e]		7.894[e]	7.974[e]
	7.8815[f]		7.881[f]	
c(Å)	**6.912**	**6.505**	**6.912**	**18.110**
	6.8962[b]	6.380[c]	6.9086[b]	17.857[d]
	6.880[e]		6.910[e]	18.491[e]
	6.9292[f]		6.9291[f]	
β(°)	**111.16**	**110.51**	**111.15**	**90.00**
	111.285[b]	111.29[c]	110.816[b]	90.00[d]
	111.28[e]		110.87[e]	90.00[e]
	110.994[f]		110.967[f]	
V(Å^3)	**659.06**	**331.59**	**659.04**	**497.97**
	642.78[b]	321.16[c]	658.80[b]	472.32[d]
	640.9[e]		659.8[e]	509.2[e]
	669.18[f]		669.33[f]	

[a] Unit-cell parameters optimized in this study with DFT are shown in bold font.

[b] Neutron data at 293 K for α phase and at 773 K for β phase by Ijdo et al., 2015.

[c] XRD data by Smith et al., 2014.

[d] XRD data by Gasperin, 1986. The cell was doubled along the *b* axis for direct comparison with the Z=3 cell used in present DFT calculations.

[e] XRD data at 303 K for α phase, at 748 K for β phase, and at 1323 K for γ phase by Smith et al., 2015.

[f] DFT by Smith et al., 2017.

The optimized structure of α-$Na_2U_2O_7$ crystallizing in a monoclinic unit cell, space group $P2_1/a$ (IT No. 14, Z = 4), has lattice parameters of a = 13.024 Å, b =7.850 Å, c = 6.912 Å (b/a = 0.603, c/a = 0.531), and β = 111.16°, consistent with the recent values of a = 12.7617(14) Å, b =7.8384(10) Å, c = 6.8962(9) Å (b/a = 0.6142, c/a = 0.5404), and β = 111.285(9)° measured at 293 K by Ijdo et al. (2015). Good overall agreement is observed between experimental and DFT-simulated X-ray diffraction patterns (Fig. 8).

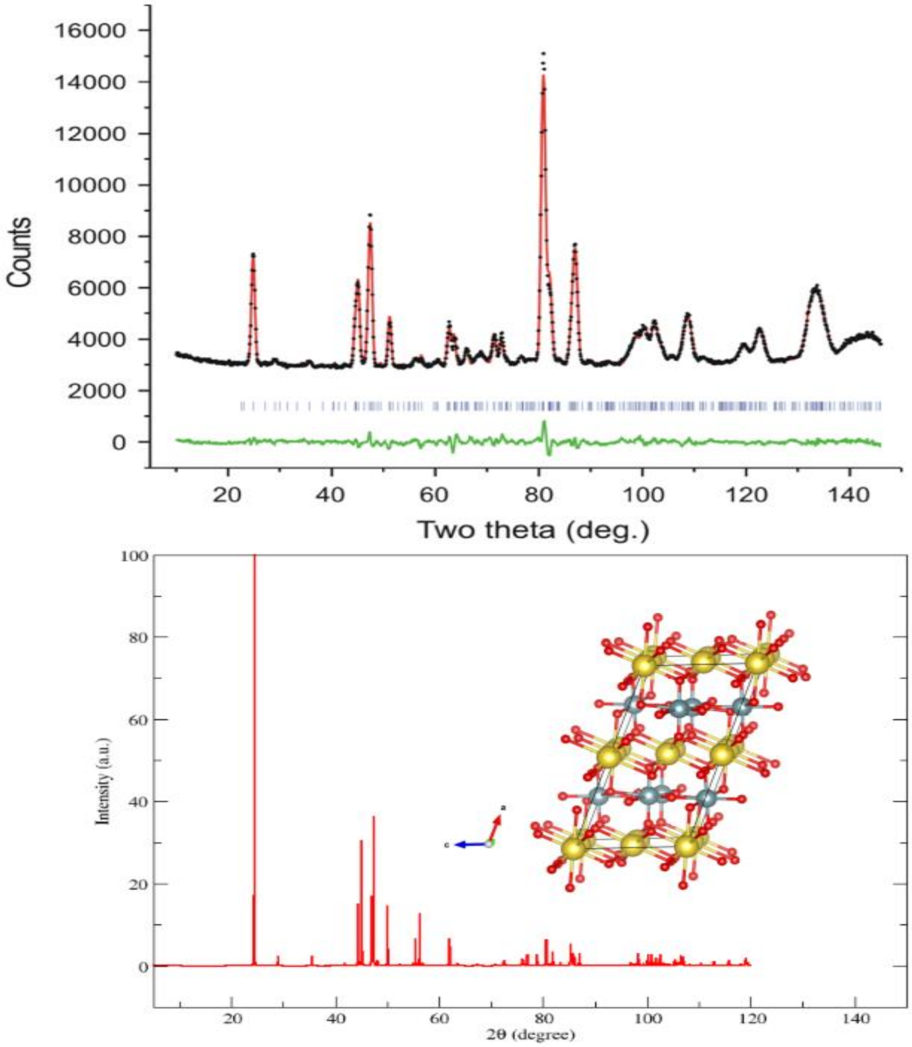

Figure 8. X-ray diffraction pattern of α-$Na_2U_2O_7$ with $P2_1/a$ symmetry (IT No. 14, Z = 4). Top: experimental diffraction pattern measured at 293 K after Ijdo et al. (2015); vertical tick marks below the profile indicate the positions of the Bragg reflections and difference (observed – calculated) curve (green) appears at the bottom of the plot. Bottom: diffraction pattern simulated from the structure relaxed with DFT/PBE reported in the present study DFT at the GGA/PBE level of theory; Insert: relaxed crystal unit cell of α-$Na_2U_2O_7$ with $P2_1/a$ symmetry. Color legend: Na, yellow; O, red; U, teal.

The relaxed structure of α-$Na_2U_2O_7$ adopting the monoclinic space group $P2_1$ (IT No. 4, Z = 2) exhibits lattice parameters of a = 6.909 Å, b = 7.877 Å, c = 6.505 Å (b/a = 1.140, c/a = 0.942), and β = 110.51^o, close to the XRD values of a = 6.887(3) Å, b = 7.844(3) Å, c = 6.380(3) Å (b/a = 1.139, c/a = 0.926) and β = 111.29(5)^o measured at room-temperature by Smith and coworkers (Smith et al., 2014). Experimental and DFT-simulated X-ray diffraction patterns are shown in Fig. 9.

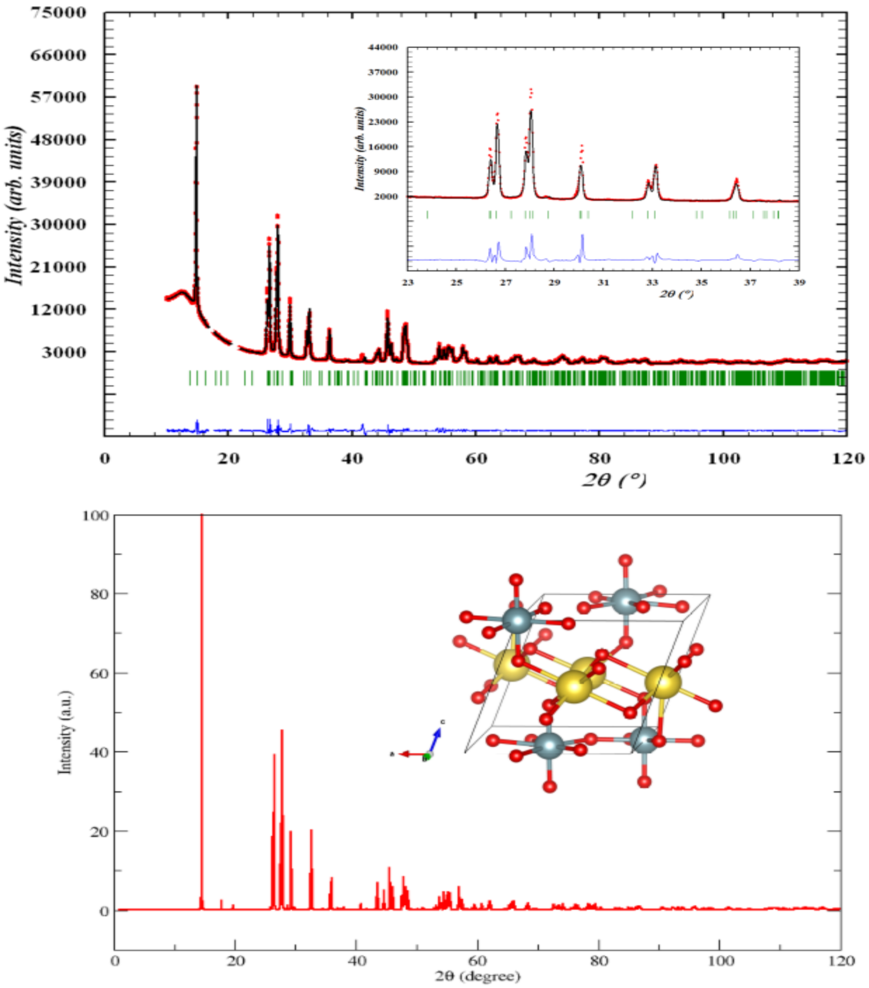

Figure 9. X-ray diffraction pattern of α-$Na_2U_2O_7$ with $P2_1$ symmetry (IT No. 4, Z = 2). Top: experimental diffraction pattern measured at room-temperature after Smith and coworkers (Smith et al., 2014); vertical tick marks below the profile indicate the positions of the Bragg reflections and difference (observed-calculated) curve (blue) appears at the bottom of the plot. Bottom: diffraction pattern simulated from the structure relaxed with DFT/PBE reported in the present study DFT at the GGA/PBE level of theory; Insert: relaxed crystal unit cell of α-$Na_2U_2O_7$ with $P2_1$ symmetry. Color legend: Na, yellow; O, red; U, teal.

The monoclinic β-$Na_2U_2O_7$ polymorph with C2/*m* symmetry (IT No. 12, Z = 4) is nearly identical to the $P2_1/a$ α-$Na_2U_2O_7$ structure, and its optimized lattice parameters are $a = 13.022$ Å, $b = 7.850$ Å, $c = 6.912$ Å ($b/a = 0.603$, $c/a = 0.531$) and $\beta = 111.15^{\circ}$, in close agreement with the XRD values of $a = 12.933(1)$ Å, $b = 7.887(1)$ Å, $c = 6.9086(8)$ Å ($b/a = 0.610$, $c/a = 0.534$) and $\beta = 110.816(10)^{\circ}$ reported at 773 K by Ijdo et al. (2015). A comparison between experimental and DFT-simulated X-ray diffraction patterns is displayed in Fig. 10.

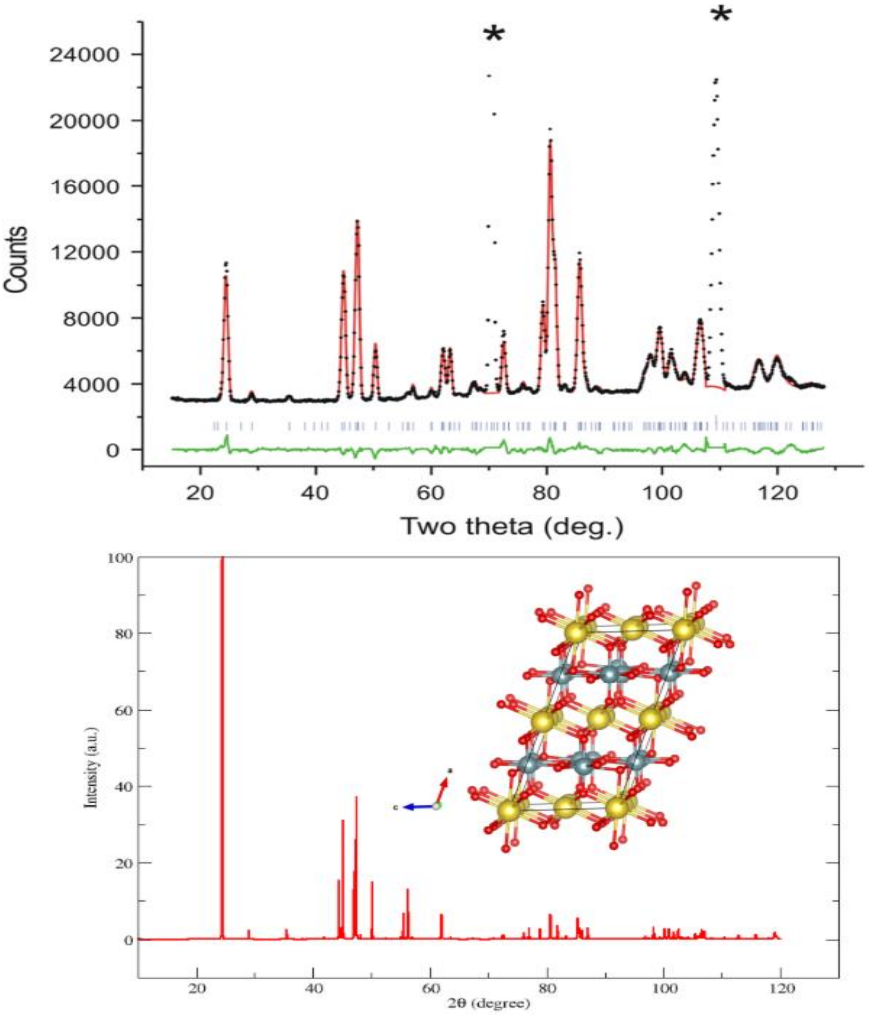

Figure 10**.** X-ray diffraction pattern of β-$Na_2U_2O_7$ with C2/*m* symmetry (IT No. 12, Z = 4). Top: experimental diffraction pattern measured at 293 K after Ijdo et al. (2015); vertical tick marks below the profile indicate the positions of the Bragg reflections; large asterisks indicate the position of the Bragg reflections of the Mo sample container. Difference (observed-calculated) curve (green) appears at the bottom of the plot. Bottom: diffraction pattern simulated from the structure relaxed with DFT/PBE reported in the present study DFT at the GGA/PBE level of theory; Insert: relaxed crystal unit cell of β-$Na_2U_2O_7$ with C2/*m* symmetry. Color legend: Na, yellow; O, red; U, teal.

The relaxed structure of γ-$Na_2U_2O_7$ adopting the R-3m symmetry (IT No. 166, Z = 3) features computed lattice parameters of *a* = 3.984 Å and *c* = 18.110 Å (*c*/*a* = 4.546), and γ = 120.06°, close to the pure, single crystal characterized by Gasperin, with lattice parameters of *a* = 3.911(3) Å and *c* = 17.857(5) Å (*c*/*a* = 4.565) (Gasperin, 1986), and similar to the clarkeite sample analyzed by Finch and Ewing, featuring lattice parameters of *a* = 3.954(4) Å and *c* = 17.73(l) Å (*c*/*a* = 4.484) (Finch and Ewing, 1997). Compared to the anhydrous form of γ-$Na_2U_2O_7$ synthesized by Gasperin and the model used in this study, the natural crystalline clarkeite sample is slightly elongated along the *a* axis and shortened along the *c* axis, probably due to the presence of residual water. As shown in Fig. 11, the diffraction pattern simulated from the structure relaxed with DFT/PBE in the present study DFT is very similar to the experimental diffraction pattern measured for clarkeite.

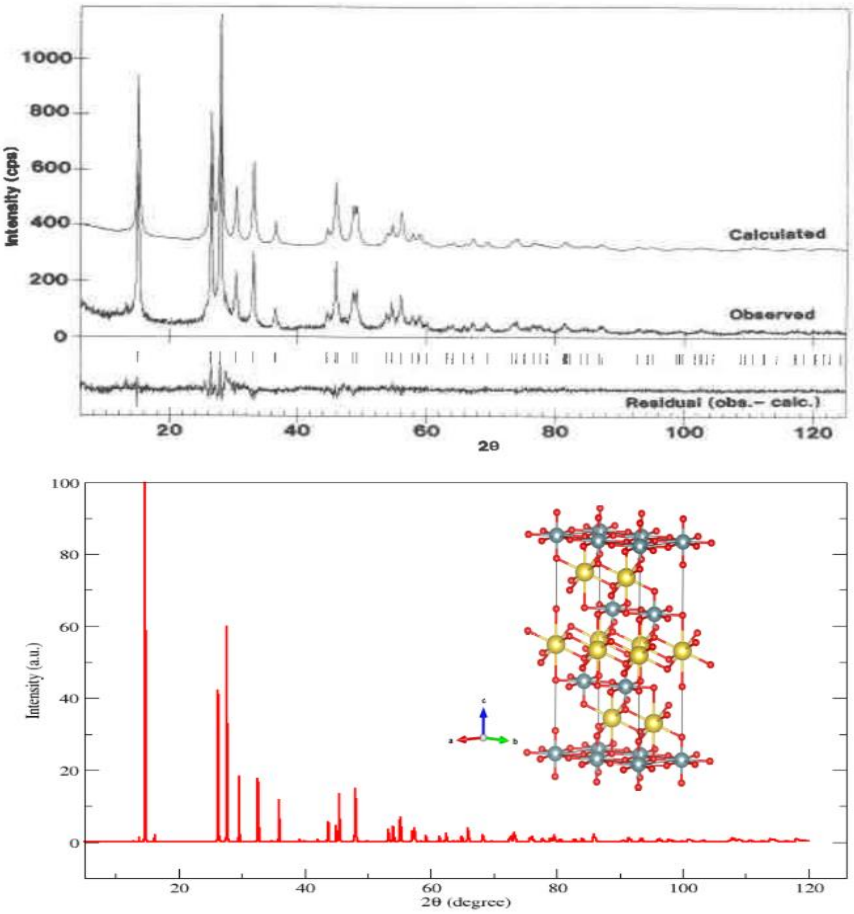

Figure 11. X-ray diffraction pattern of γ-$Na_2U_2O_7$ with R-3m symmetry (IT No. 166, Z = 3). Top: experimental diffraction pattern measured for clarkeite after Finch and Ewing (1997); vertical tick marks below the profile indicate the positions of the Bragg reflections and difference (observed-calculated) curve appears at the bottom of the plot. Bottom: diffraction pattern simulated from the structure relaxed with DFT/PBE reported in the present study DFT at the GGA/PBE level of theory; Insert: relaxed crystal unit cell of γ-$Na_2U_2O_7$ with R-3m symmetry. Color legend: Na, yellow; O, red; U, teal.

DFT Gibbs free energies and heat capacities of $Na_2U_2O_7$ polymorphs

The thermal evolutions of the Gibbs free energy of the of α-$Na_2U_2O_7$ with $P2_1/a$ and $P2_1$ symmetries, β-$Na_2U_2O_7$ with C2/*m* symmetry, and γ-$Na_2U_2O_7$ with R-3m symmetry predicted using DFPT/QHA are displayed in Fig. 12. Calculations predict that α-$Na_2U_2O_7$ with $P2_1/a$ symmetry and β-$Na_2U_2O_7$ are energetically degenerate at low temperature, with Gibbs energy differences of ~1 meV. As the temperature increases, the β-$Na_2U_2O_7$ tend to become slightly more stable than $P2_1/a$ α-$Na_2U_2O_7$, which is consistent with the observation of a α → β phase transition at above ~600 K by Smith and coworkers (Smith et al., 2015) and by Cordfunke et al. (Cordfunke and Loopstra, 1971; Cordfunke et al., 1982). Since the energy difference between both phases is only ~0.015 eV at 600 K, this α → β phase transition is predicted to be rather sluggish; this finding is in line with the experimental characterization by Kovba (1972), and by Cordfunke et al. (1982), and by Ijdo et al. (2015), who all reported slow kinetics for the α → β phase transition. In addition, calculations show that at low temperature, the α-$Na_2U_2O_7$ structure adopting the monoclinic space group $P2_1$ reported by Smith and coworkers (Smith et al., 2014) is only slightly less energetically favorable than the α-$Na_2U_2O_7$ with $P2_1/a$ symmetry; the difference in Gibbs free energy of α-$Na_2U_2O_7$ with $P2_1/a$ and $P2_1$ symmetries is less than ~0.04 eV near the zero-temperature limit. Therefore, it can be inferred that the metastable $P2_1$ α-$Na_2U_2O_7$ characterized by Smith et al. might eventually decay into $P2_1/a$ α-$Na_2U_2O_7$ or a mixture of $P2_1/a$ α-$Na_2U_2O_7$ and β-$Na_2U_2O_7$ phases. Similarly, calculations show that the pure γ-$Na_2U_2O_7$ phase with R-3m symmetry is metastable at low temperature, with respect to the $P2_1/a$ α-$Na_2U_2O_7$ and β-$Na_2U_2O_7$ phases. This explains why pure γ-$Na_2U_2O_7$ phase synthesized at high temperature (i.e., above ~1200 ^{o}C by Gasperin) must be rapidly quenched to room temperature for crystallographic characterization; as reported by Smith et al. (Smith et al., 2015), gradual cooling of γ-$Na_2U_2O_7$ to room temperature of what was expected to be either pure β-$Na_2U_2O_7$ or γ-$Na_2U_2O_7$, resulted instead in a mixture of α and β phases.

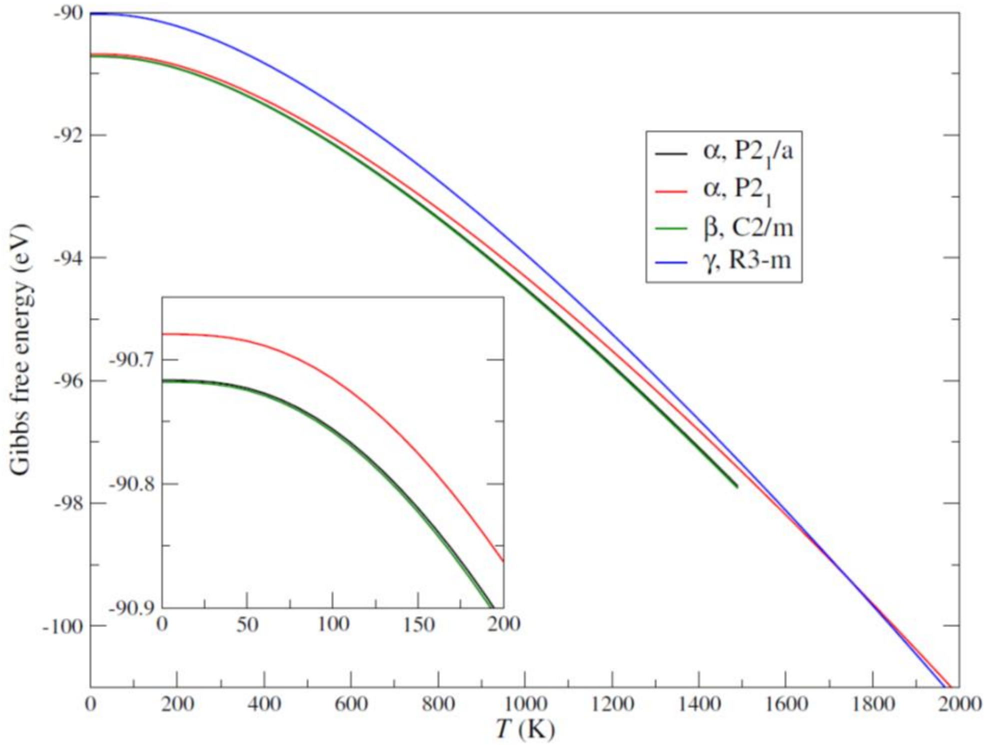

Figure 12. Variations of the Gibbs free energy of α-$Na_2U_2O_7$ with $P2_1/a$ and $P2_1$ symmetries, β-$Na_2U_2O_7$ with C2/*m* symmetry, and γ-$Na_2U_2O_7$ with R-3m symmetry computed with DFPT at the GGA/PBE level, within the QHA approximation.

Although early experimental investigations reported the existence of a β-$Na_2U_2O_7$→ γ-$Na_2U_2O_7$ phase transition at 1348 K (Cordfunke and Loopstra, 1971; Cordfunke et al., 1982), which was recently observed with XRD to be in the range 1223-1323 K by Smith and coworkers (Smith et al., 2015), DFT calculations using pure, stoichiometric β-$Na_2U_2O_7$ and γ-$Na_2U_2O_7$ phases do not lend support to this interpretation. As shown in Fig. 12, the Gibbs free energy curves for the $P2_1/a$ α-$Na_2U_2O_7$ and β-$Na_2U_2O_7$ phases do not cross that of the γ-$Na_2U_2O_7$ phase, therefore no temperature-driven $P2_1/a$ α-$Na_2U_2O_7$ or β-$Na_2U_2O_7$→ γ-$Na_2U_2O_7$ phase transition is expected to occur at high temperature. In addition, although the Gibbs free energy curves of the γ-$Na_2U_2O_7$ phase and the metastable $P2_1$ α-$Na_2U_2O_7$ phase do cross at ~1743 K (Fig. 12), experiments by

Smith et al. (2015) indicated that γ-$Na_2U_2O_7$ is completely decomposed around ~1620 K according to the reaction $Na_2U_2O_7$(cr) → 2UO_2(cr) + Na(g) + ½ Na_2O(g) + 5/4 O_2(g), with further vaporization of UO_2 product occurring above ~1755 K. Therefore, this rules out the occurrence of a possible interconversion between the $P2_1$ α-$Na_2U_2O_7$ phase and γ-$Na_2U_2O_7$. Other mechanisms might be at play in the observed β-$Na_2U_2O_7$→ γ-$Na_2U_2O_7$ phase transition (e.g., defect creation, possible presence of an intermediate phase or a mixture of phases in the 1223-1323 K temperature range). Nevertheless, the present DFT calculations confirms that β-$Na_2U_2O_7$ is the most stable phase up to at least 1223 K, in agreement with the experiments by Smith et al. (2015) which show that β-$Na_2U_2O_7$ is stable between ~748 and ~1223 K. More work is needed to explain details of the β-$Na_2U_2O_7$→ γ-$Na_2U_2O_7$ phase transition, although this high-temperature range is beyond thermal conditions typically encountered in process vessels and transfer pipes at nuclear waste storage tank farms.

Fig. 13 shows the thermal variations of the molar isobaric heat capacity, C_P, of α-$Na_2U_2O_7$ with $P2_1/a$ and $P2_1$ symmetries, β-$Na_2U_2O_7$ with C2/*m* symmetry, and γ-$Na_2U_2O_7$ with R-3m symmetry predicted in this study with DFPT at the GGA/PBE level, within the QHA approximation. The experimental values of the molar isobaric heat capacity measured by Cordfunke et al. (1982), and the corresponding DFT results by Smith and coworkers (Smith et al., 2017) using the CASTEP code for α-$Na_2U_2O_7$ ($P2_1/a$) and β-$Na_2U_2O_7$ (C2/*m*) are also depicted in Fig. 13. Similar to the entropy *S* and isochoric heat capacity C_V of $P2_1$ α-$Na_2U_2O_7$ calculated as part of FY21 modeling activities related to waste form degradation (Jové Colón et al., 2021), the C_P values predicted are systematically much smaller than the corresponding predictions for other polymorph structures. Except for γ-$Na_2U_2O_7$, the C_P values for α- and β-$Na_2U_2O_7$ calculated here are smaller than calorimetric data by Cordfunke and coworkers (Cordfunke et al., 1982). The experimental reference standard molar isochoric heat capacity measured by Cordfunke et al. is $C_P{}^o{}_m$ (298.15 K) = 227.26 J $K^{-1}mol^{-1}$, while the values predicted by Smith and coworkers (Smith et al., 2017) for α-$Na_2U_2O_7$ ($P2_1/a$) and β-$Na_2U_2O_7$ (C2/*m*) are $C_P{}^o{}_m$ = 229.5 (+1.0%) and 230.6 (+1.5%) J $K^{-1}mol^{-1}$, respectively. Let us note that, based on the results and discussion of Fig. 12, it can be inferred that the calorimetric data by Cordfunke et al. correspond to an actual mixture of for α-$Na_2U_2O_7$ ($P2_1/a$) and β-$Na_2U_2O_7$ (C2/*m*), instead of a pure α-$Na_2U_2O_7$ phase. Here, the predicted standard values of $C_P{}^o{}_m$ are 212.0 (-6.7%), 219.4 (-3.4%), 220.9 (-2.8%), and 226.6 (-0.3%) J $K^{-1}mol^{-1}$ for $P2_1$ α-$Na_2U_2O_7$, $P2_1/a$ α-$Na_2U_2O_7$, C2/*m* β-$Na_2U_2O_7$, and *R*-3m γ-$Na_2U_2O_7$, respectively. With the exception of $P2_1$ α-$Na_2U_2O_7$, including the effect of volume change upon heating in $C_P{}^o{}_m$ tend to improve agreement with experiment, compared to previous values of $C_V{}^o{}_m$ (298.15 K), which were predicted to be 213.0 (-6.3%), 217.5 (-4.3%)], 217.5 (-4.3%), and [217.4 (-4.3%) J $K^{-1}mol^{-1}$ for $P2_1$ α-$Na_2U_2O_7$, $P2_1/a$ α-$Na_2U_2O_7$, C2/*m* β-$Na_2U_2O_7$, and *R*-3m γ-$Na_2U_2O_7$, respectively (Jové Colón et al., 2021).

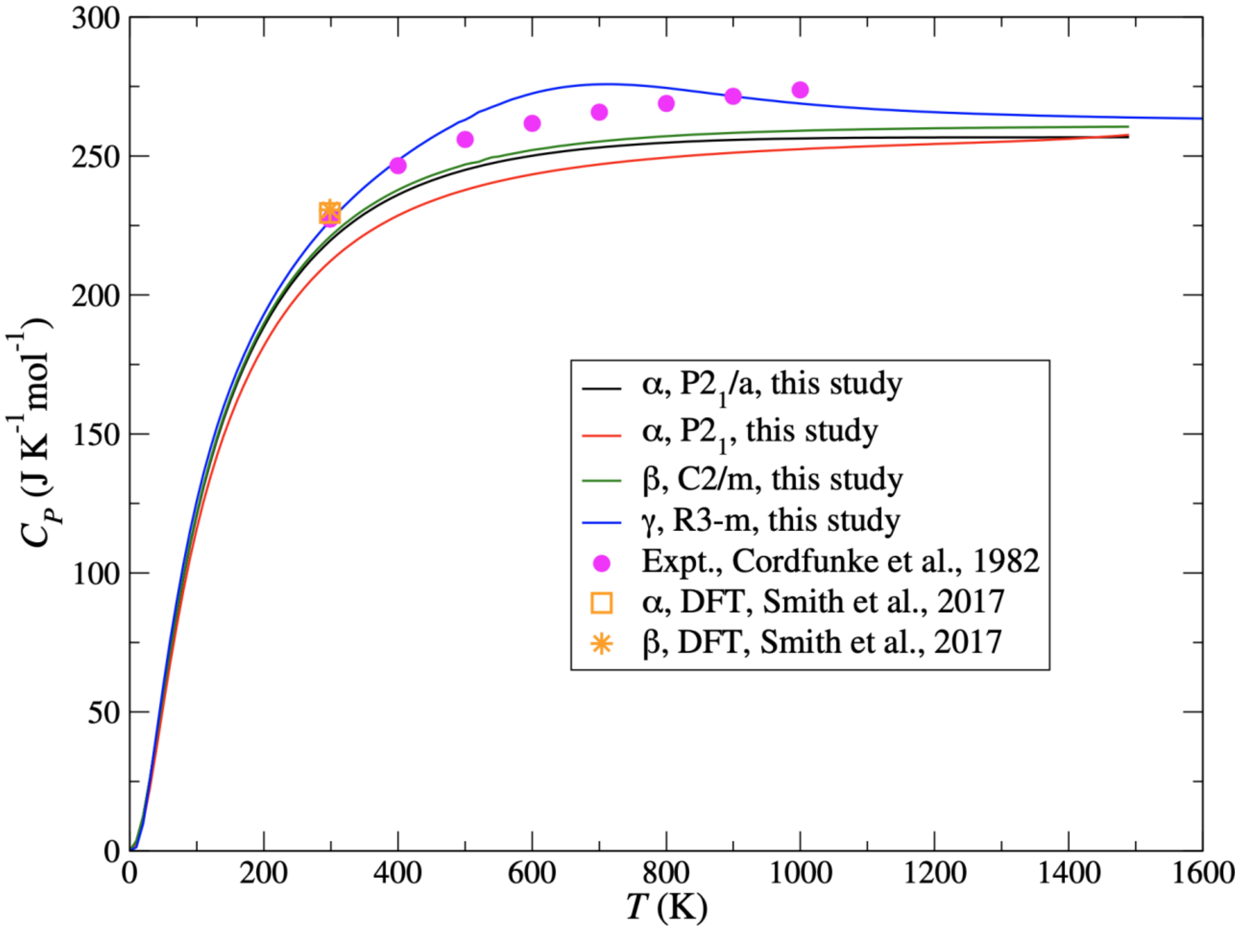

Figure 13. Thermal evolution of the molar isobaric heat capacity, C_P, of α-$Na_2U_2O_7$ with $P2_1/a$ and $P2_1$ symmetries, β-$Na_2U_2O_7$ with C2/*m* symmetry, and γ-$Na_2U_2O_7$ with R-3m symmetry computed with DFPT at the GGA/PBE level. The experimental values of the molar isobaric heat capacity measured by Cordfunke et al. (1982), and the corresponding DFT results by Smith and coworkers (Smith et al., 2017) for α-$Na_2U_2O_7$ ($P2_1/a$) and β-$Na_2U_2O_7$ (C2/*m*) are also displayed for comparison.

Conclusions

In summary, first-principles methods based on DFT/DFPT were utilized to provide an independent assessment of existing experimental structural and thermodynamic data and possibly resolve contradictions in existing data in the Na-U-O system. In particular, as mentioned in previous studies, there has not been a clear consensus on the structures and relative thermal stabilities of $Na_2U_2O_7$ polymorphs. To avoid inadvertent precipitation, crystallization, and accumulation of uranium phases in process vessels and transfer pipes at nuclear waste storage tank farms, a comprehensive computational analysis of the complex relationships between crystal structures and thermodynamic stability of $Na_2U_2O_7$ polymorphs was carried out during FY22, with systematic experiment-theory comparison.

As a continuation of FY21 modeling activities related to waste form degradation, these calculations were conducted to predict volume-dependent phonon properties, Gibbs free energies and isobaric heat capacities of the α-, β-, and γ-$Na_2U_2O_7$ polymorphs for direct comparison with calorimetric data. Comparison between simulated XRD diffraction patterns using optimized DFT models showed overall good agreement with measured experimental diffraction patterns of α- and β-$Na_2U_2O_7$, as well as clarkeite. Calculations predict that α-$Na_2U_2O_7$ with $P2_1/a$ symmetry and β-$Na_2U_2O_7$ are energetically degenerate at low temperature, with Gibbs energy differences of ~1 meV. As the temperature increases, the β-$Na_2U_2O_7$ tend to become slightly more stable than $P2_1/a$ α-$Na_2U_2O_7$, which is consistent with the observation of a α → β phase transition at above ~600 K. Since the energy difference between both phases is only ~0.015 eV at 600 K, this phase transition is predicted to be rather sluggish, in line with experimental characterization. At low temperature, the $P2_1$ α-$Na_2U_2O_7$ structure is only slightly less energetically favorable than the $P2_1/a$ α-$Na_2U_2O_7$, suggesting that metastable $P2_1$ α-$Na_2U_2O_7$ might eventually decay into $P2_1/a$ α-$Na_2U_2O_7$ or a mixture of $P2_1/a$ α-$Na_2U_2O_7$ and β-$Na_2U_2O_7$ phases. Similarly, calculations show that pure γ-$Na_2U_2O_7$ with R-3m symmetry is metastable at low temperature, with respect to the $P2_1/a$ α-$Na_2U_2O_7$ and β-$Na_2U_2O_7$ phases. Although DFT calculations confirm that β-$Na_2U_2O_7$ is the most stable phase up to at least 1223 K, the existence of a β-$Na_2U_2O_7$→ γ-$Na_2U_2O_7$ phase transition at high temperature could not be confirmed by calculations using pure, stoichiometric β-$Na_2U_2O_7$ and γ-$Na_2U_2O_7$ phases. More work is needed to explain details of the β-$Na_2U_2O_7$→ γ-$Na_2U_2O_7$ phase transition.

In FY23, this methodology will be applied to other crystalline systems (e.g., other uranium-bearing minerals, montmorillonite clays) to expand the applicability of this data set to realistic systems. Such an expanded data set will facilitate investigation of NS, EBS and SNF thermal-mechanical evolution at nuclear storage sites and in geological repositories.

IV. Electrochemical Modeling of UO_2 Spent Nuclear Fuel (SNF)

An example of a zero-D electrochemical corrosion interaction model representing a liquid bath reservoir cell with UO_2 is illustrated in Fig. 14. The zero-D reactor model represents a series of interconnected reactors with inlets and outlets. This model is built on the Zuzax code suite developed at SNL (Moffat and Jové Colón, 2009). Zuzax is a general purpose, object-oriented constitutive modeling package with applications to electrochemical processes in corrosion and Gibbs energy minimization problems in multicomponent multiphase equilibria. The code suite can be used to describe solution-solid equilibria using various types of activity coefficient models (e.g., Pitzer, extended Debye-Huckel) extending its capability from dilute solutions to concentrated brine systems.

The reactor model is being developed to represent key components of electrochemical corrosion systems with interfaces such as metal electrode volume, Butler-Volmer charge transfer with general surface reaction mechanisms, gas transport though an interface, thermodynamics of uranium aqueous speciation/solution chemistry, and diffusion with respect to electrochemical potential. This year, we have migrated the UO_2 half-cell and full cell model into the zero-D framework within Zuzax, which has been documented in a Sandia report (Moffat and Jové Colón, 2021), and is also currently being used to model electroplating systems.

In contrast to many thermodynamic databases in the geochemistry field, Zuzax' thermochemistry formulation is based on the modified NIST-JANAF/NASA (Chase et al, 1998) assumption that the heat of formation of elements in their standard states at 298K and one bar are equal to zero. The modification to that standard involves the electron element heat of formation standard. Instead of the gas ionization of hydrogen standard used by NIST, Zuzax' electron formulation is based on the adherence to the standard hydrogen electrode (SHE) as a function of temperature and pressure (Ives et al., 1961). This means, in practice, that the E_o's produced by the Zuzax thermochemistry can be compared directly to the CRC values. Also, the thermodynamics produced for solid and gas species can be compared directly to and augmented by the JANAF table values (Chase et al, 1998).

This year, the thermochemistry formulation has been expanded to include a JSON reader, for the eventual inclusion of data from the THEREDA thermodynamic database (https://www.thereda.de/en/), which includes extensive data for actinide thermodynamics (Moog, 2015). Internal calculations to reproduce a JANAF standard thermodynamic formulation from THEREDA's formation reaction approach are currently in progress. Eventual inclusion of other databases such as the NEA database are also anticipated in the future (Ragoussi and Costa, 2019), using the same approach as employed in THEREDA's thermodynamic database implementation.

Zuzax can also evaluate electrochemical reactions with kinetics. Given its history in model implementation to evaluate electrochemical systems, it provides for a robust modeling platform to develop corrosion models aimed at capturing system feedbacks with changes in solution chemistry. Such model development is key to the assessment of in-package chemistry in process models in the evaluation of the source term. Descriptions of the reactor class development to evaluate SNF (UO_2) corrosion follows the Sandia Report (Moffat and Jové Colón, 2021), but are also given in the following section.

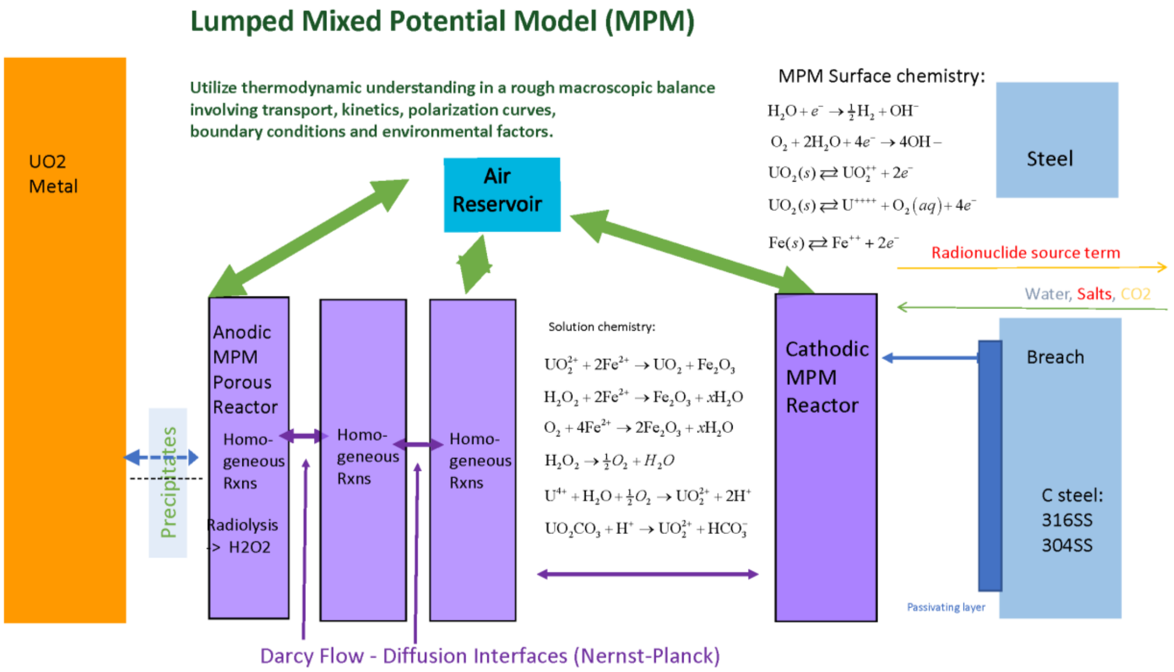

Figure 14. Schematic diagram of the zero-D reactor network model for UO_2 corrosion using the Zuzax code suite.

Half-Cell Equation Set

The half-cell reactions involve specifying a voltage drop across the cell. The implementation takes place within Zuzax using a `ChargedFluidReactor` reactor class described in the report (Moffat and Jove-Colon, 2021). The `ChargedFluidReactor` reactor is designed to solve electrochemical reactions systems within a small or stirred cell filled with an ionic liquid such as an aqueous brine that is bounded by metal interfaces, air-water interfaces and other `ChargedFluidReactor` cells with which the cell exchanges species and net current using a transport operator with an electric potential gradient. The `SubstrateElement` reactor is used for the UO_2 anode, which undergoes anodic dissolution.

The time-dependent equations must be solved using the differential algebraic equation (DAE) integrator, because the voltage equation is provided as an algebraic constraint. Before the DAE solver is started, the initial conditions for the algebraic constraints, the specification of the electric potentials of the brine control volumes must be calculated first, using a special non-linear solver built for that purpose that is built into Zuzax's reactor network modeling capability.

This is an essential step, because errors in the electric potential from the algebraic constraint may cause Bulter-Volmer electrode reactions to extend outside the linear region into the exponential Tafel-slope region, leading to large deviations in the residual and causing ill-conditioned matrices that can't be successfully solved. More often than not, the first time step within DAE system cannot be successful solved, unless the initial electric potentials are solved for first.

The main equations are somewhat modeled after `ConstantPressureIdealGas`. The volume is calculated from the natural volume of all of the phases in the `PhaseList.` The pressure of each cell is assumed to be constant. Because there is no imposed net pressure differences across the domain, there is no need to include Darcy flow in the simulation, yet. An expansion of the reactor network to reactors employing Darcy flow within a multicomponent porous network is scheduled for the modeling effort this year. For current problems of interest, the temperature is kept at a constant and no energy equation is solved. Also, all conservation equations are written in terms of the total moles of each species in kmol units.

The unknowns solved for all involve neutral combinations of ions, after first defining a major cation and anion for the system. This leads to a more stable solution algorithm as well as a reduction in the number of equations for each domain of one. This component unknown approach is fully described in Section 3.10 of (Moffat and Jove-Colon, 2021).

The conservation equation for the number of kmoles of species k in the reactor R, $n_{R,k}$, can be written down as Eqn. (1).

$$\frac{d(n_{R,k})}{dt} = V_R \dot{W}_k + \dot{F}_{R,inlet} X_{R,k}^{inlet} - \dot{F}_{R,outlet} X_{R,k} + \sum_{face} A_{R,face} \boldsymbol{n}_R \cdot \dot{\boldsymbol{F}}_{k,face} + \sum_I A_{R,I} \dot{S}_{R,I,k}$$
$$k = 1, \dots, N^{lyte} \tag{1}$$

In Eqn. (1), $n_{R,k}$ is the number of kmols of species k in the half-reactor R. N^{lyte} is the number of species in the electrolyte brine phase, including water. $\dot{W}_k$ is the source term due to homogeneous reactions within the reactor R (kmol/m^3/s). V_R is the volume of reactor R. $\dot{S}_{R,I,k}$ is the source term for species k for the reactor R from the I^{th} interface. Interfaces for the reactor equation include an electrode interface between the brine and the UO_2 spent fuel package, and an interface between the brine and an air reservoir, allowing for equilibration of an air phase with the brine phase, mitigated by a mass transport limitation given by a difussion boundary layer thickness.The air phase allows for interphase transport of O_2, H_2O, and CO_2.

$F_{k,face}$ is the areal diffusional and capillary advective flux of species *k* across a diffusional interface *D*, with surface area $A_{R,D}$. $\boldsymbol{n}_R$ is the outward facing unit normal to the half-cell domain R. We have chosen to separate out the diffusional interfaces from the reaction interfaces in this formulation of the problem, though the diffusional interfaces are just a child class of the reaction interfaces.

A bath reservoir cell is defined as an infinite source for solution at a specified concentration, temperature, pressure, and electric potential. This is what specifies the needed conditions to fully define the half-cell.

In order to complete the specification and to avoid conflict with the equation for v_D and in the absence of a Darcy flow formulation with a specified reactor volume, the advection velocity of diffusional flows is specified in some manner. Typically, the net solvent velocity is set to zero allowing for net solute transport to occur with a net volume change in the reactor, at constant pressure. A constant volume case is also possible, where the volume of the reactor is kept at a specified constant, with an added forced advection velocity added to a diffusional interface needed to be added to fully specify the formulation. Additionally, with this capability, there must exist one `ChargedFlowReactor` in the network that operates on a constant pressure basis so that modified total volume of the brine phase may be accommidated by that reactor. The equation for specification of the forced advection velocity is given by Eqn. (2), which is an expression of the net volume of the reactor not changing. $\overline{V}_k$ is the molar volume of species *k*, with nucleating solid phases also included in the summation.

$$\sum_{k=1}^{Nt} \frac{d\left(n_{R,k}\overline{V}_k\right)}{dt} = 0 \tag{2}$$

The voltage equation is based on the algebraic equation asserting that net sum of all charge fluxes into the cell, *R*, is equal to zero, Eqn. (3). This relation, in combination with the initial conditions that asserts charge neutrality, maintains the charge neutrality of the brine phase by setting the net charge flux into the domain to be zero at all times. The unknown corresponding to this equation is the voltage of the brine phase within the cell.

$$\sum_k \sum_I A_{R,I} \dot{S}_{R,I,k} z_k + \sum_k \sum_D A_{R,D} n_R \dot{F}_{k,face} z_k = 0 \tag{3}$$

Note, $\dot{F}_{k,face}$ is the diffusional and convective flux of species *k* across the face from the diffusional face interface, *D*, which is connected to another `ChargedFluidReactor` cell or to the bath solution reactor. $N_R$is the normal component of the face that points into the *R* cell. z_k is the charge of the *k*th species.$n_{Rj}\dot{F}_{k,face}$is the source input of species *k* into the R cell from a neighboring cell or from a neighboring bath cell.

The above equation must be coupled to a treatment where the velocity is defined as the molar average velocity and the diffusion operator is defined with respect to the molar average velocity.

The total diffusive flux at the interface is given by the following expression,

$$\boldsymbol{J}_k^I = \boldsymbol{v}_{corr}^{vol} c_k^l + \boldsymbol{J}_k^{I,uncorr} = \boldsymbol{v}_{corr}^{vol} c_k^l - D_k \nabla c_k^L - D_k c_k^L \frac{z_k F}{RT} \nabla \phi \tag{4}$$

Here we add a velocity correction, $\boldsymbol{v}_{corr}^{vol}$, to the diffusive flux, Eqn. (4), so that the net volumetric flow due to diffusion is equal to zero. $\bar{V}_k$is defined as the partial molar volume of species *k*. The velocity correction vector for a volumetric reference velocity is given by Eqn. (5).

$$\begin{aligned} \boldsymbol{v}_{corr}^{vol} &= -\sum_k J_k^{I,uncorr}\bar{V}_k = \sum_k \left(-\bar{V}_k D_k \nabla c_k^L - D_k \bar{V}_k c_k^L \frac{z_k F}{RT} \nabla \phi \right) \\ &= \sum_k \left(-\bar{V}_k D_k \nabla c_k^L - D_k \frac{\bar{V}_k X_k}{\bar{V}} \frac{z_k F}{RT} \nabla \phi \right) \end{aligned} \tag{5}$$

The net volume velocity reference frame description is a pertinent definition of diffusion in these types of simulations. However, we have also used a solvent velocity reference frame condition where we assign the solvent diffusive flux to being zero, Eqn. (6).

$$\boldsymbol{J}_0^I = 0 \tag{6}$$

The total flux at the interface is given by the following additional expression, where v_D is defined as the advection velocity for the simulation. It can be equated to Darcy velocity if the equations are translated into a porous flow formulation. Or, it can be solved for using Eqn. (2), which is used for a constant volume reactor.

$$\boldsymbol{N}_k^I = \boldsymbol{v}_D c_k^l + \boldsymbol{J}_{\boldsymbol{k}}^{\boldsymbol{l}} \tag{7}$$

Eqn. (7) suffers from the possibility of instability for cell Peclet numbers greater than 2. Consider the expression for the flux of species k up all of the terms for each species in the expression,

$$\begin{aligned} N_k^I &= v_D c_k^l + v_{corr}^{vol} c_k^l - D_k \nabla c_k^L - D_k c_k^L \frac{z_k F}{RT} \nabla \phi \\ &= c_k^l \left(v_D + v_{corr}^{vol} - D_k \frac{z_k F}{RT} \nabla \phi \right) - D_k \nabla c_k^L \end{aligned} \tag{18}$$

The bottom line of Eqn. (18) demonstrates that the advective velocity includes additional terms other than the simple advective velocity, most notably including the electric migration velocity due to the imposed electric field, which is dependent on the charge, and may be directed in different directions according to the charge on the species. We define the commulative advection velocity for species k, $\boldsymbol{v}_k^{adv}$, as the sum of the terms inside the parentheses of Eqn. (8).

$$\boldsymbol{v}_k^{adv} = \left(v_D + v_{corr}^{vol} - D_k \frac{z_k F}{RT} \nabla \phi \right) \tag{9}$$

Then, a proper first order upwinding treatment of Eqn. (8), which is all that is necessary for this macroscopic balance treatment of the UO$_2$ system, would formally be written as.

$$N_k^I = \boldsymbol{v}_k^{adv} [\![c_k^l, \boldsymbol{v}_k^{adv}]\!]_{-,+} - D_k \nabla c_k^L \tag{8}$$

where,

$$[\![X_k, \mathrm{v}]\!]_{-,+} = \begin{cases} X_-, & \mathrm{v} \cdot \mathrm{n} > 0 \\ X_+, & \mathrm{v} \cdot \mathrm{n} < 0 \end{cases}$$

and X_- is the value on the negative side of the interface (i.e., left side) and X_+ is the value on the positive side of the interface (i.e., the right side). In other words, this is the standard upwards differencing of the advection term. We have found that this treatment of the advection term for the reactor equations is necessary for the maintenance of a maximum principle within the equation system.

In future work, we will string multiple half cells together to create a one-dimensional domain to better resolve the diffusion gradient. However, this work is meant to be focused on the overall macroscopic balances, trying to understand the important reaction mechanisms and constitutive relations that drive the general system. In addition, the zero-D model will incorporate the formation of solid precipitates in the reactor network.

V. FY2023 Work

Planned work on wasteform modeling for FY23 (and the remainder of FY22):

Glass degradation Stage III modeling:

- Further expand reaction path modeling and analysis to evaluate rate law parameter sensitivities on secondary phase formation and solute concentrations glasses with Stage III resumptive dissolution trends.
- Continue evaluation of various combinations of mineral inclusions/suppressions focusing on secondary aluminosilicates formation and their effect on the resulting temporal evolution of leached components (Si, Na, B, Li, etc.)

DFT studies on clarkeite:

- Calculations of the C_P of alpha-, beta- and gamma polymorphs of clarkeite to attempt to improve agreement with calorimetric data. Extend calculations to compute Gibbs energies values and evaluate the relative stability of clarkeite polymorphs.
- Complete calculations of C_P with DFPT, within the quasiharmonic approximation (QHA), to allow a meaningful direct comparison with the experimental data.
- Prepare manuscript describing this work for publication in a peer-reviewed journal.

Electrochemical modeling of UO_2 degradation

- Further expand Zuzax UO_2 electrochemical model of reactor network of multiple half cells to include an air (gas) interface and the formation solid precipitates.
- Continue testing of the Zuzax model for code stability and the correct speciation in the U(IV)-U(VI)-CO_3-H_2O system.
- Integration of this modeling effort with ANL electrochemical experiments on UO_2.

VI. References

Abraitis, P.K., B.P. McGrail, D.P. Trivedi, F.R. Livens, and D.J. Vaughan (2000). Single-pass flow-through experiments on a simulated waste glass in alkaline media at 40°C. I. Experiments conducted at variable solution flow rate to glass surface area ratio. *Journal of Nuclear Materials* **280** (2), p. 196–205. Doi: 10.1016/S0022-3115(00)00041-6.

Blanc, P., Vieillard, P., Gailhanou, H., Gaboreau, S., Gaucher, É., Fialips, C.I., Madé, B. and Giffaut, E. (2015) A generalized model for predicting the thermodynamic properties of clay minerals. *American Journal of Science* **315**, p. 734-780.

Bourcier, W.L. 1994. Waste glass corrosion modeling – Comparison with experimental results. In *Scientific Basis for Nuclear Waste Management XVII*, eds. A. Barkatt and R.A. VanKonynenburg, 69–82. Pittsburgh, PA: Materials Research Society.

Brady, P.V., B.W. Arnold, G.A. Freeze, P.N. Swift, S.J. Bauer, J.L. Kanney, R.P. Rechard, and J.S. Stein 2009. *Deep Borehole Disposal of High-Level Radioactive Waste*. SAND-2009-4401. Albuquerque, NM: Sandia National Laboratories.

Bourcier, W., Peiffer, D., Knauss, K., McKeegan, K. and Smith, D. (1989) A kinetic model for borosilicate glass dissolution based on the dissolution affinity of a surface alteration layer. Lawrence Livermore National Lab.(LLNL), Livermore, CA (United States).

Carlstrom, R.F (1977). *Ion Exchange Flowsheet for Recovery of Cesium From PUREX Sludge Supernatant at B Plant*. ARH-F-106. Atlantic Richfield Hanford Company, Richland, WA.

Carnall, W. T., A. Walker, and S. J. Neufeldt (1966). Anhydrous Sodium Polyuranates. *J. Inorg. Chem.*, **5**, 2135-2140.

Cassingham, N., C.L. Corkhill, D.J. Backhouse, R.J. Hand, J.V. Ryan, J.D. Vienna and N.C. Hyatt (2015). The initial dissolution rates of simulated UK Magnox-ThORP blend nuclear waste glass as a function of pH, temperature and waste loading. *Mineralogical Magazine* **79** (6), p. 1529–1542.

Cordfunke, E. H. P., and B. O. Loopstra (1971). Sodium Uranates: Preparation and Thermochemical Properties. *J. Inorg. Nucl. Chem.*, **33**, p. 2427-2436.

Cordfunke, E. H. P., R.P. Muis, W. Ouweltjes, H.E. Flotow, P.A.G. O'hare (1982). The Thermodynamic Properties of Na_2UO_4, $Na_2U_2O_7$, and $NaUO_3$ *Journal of Chemical Thermodyn*amics, **14**, p. 313-322.

Criscenti, L.J. and D. Sassani 2010. *Upscaling Atomistic Mechanisms to Continuum Models for Nuclear Waste Glass Dissolution*. FMM NEAMS Project Report/SAND-2010-6707P. Albuquerque, NM: Sandia National Laboratories.

Criscenti, L.J., S.L. Brantley, K.T. Mueller, N. Tsomaia, and J.D. Kubicki (2005). Theoretical and ^{27}Al CPMAS NMR investigation of aluminun coordination changes during aluminosilicate dissolution. *Geochimica et Cosmochimica Acta* **69** (9), p. 2205–2220.

Criscenti, L.J., J.D. Kubicki, and S.L. Brantley (2006). Silicate glass and mineral dissolution: Calculated reaction paths and activation energies for hydrolysis of a Q^3 Si by H_3O^+ using ab initio methods. *Journal of Physical Chemistry A* **110** (1), p. 198–206.

Criscenti, L.J., P.A. Schultz, C. Steefel, P. Zapol, and I. Bourg (2011). *Progress toward Bridging from Atomistic to Continuum Modeling to Predict Nuclear Waste Glass Dissolution*. SAND-2011-8250. Albuquerque, NM: Sandia National Laboratories.

Crum, J.V., Reiser, J.T., Parruzot, B.P., Neeway, J.J., Bonnett, J.F., Kerisit, S.N., Cooley, S.K., Ryan, J.V., Smith, G.L. and Asmussen, R.M. (2021) Seeded Stage III glass dissolution behavior of a statistically designed glass matrix. J Am Ceram Soc 104, 4145-4162.

Cunnane, J.C., ed.; J.K. Bates, C.R. Bradley, E.C. Buck, W.L. Ebert, X. Feng, J.J. Mazer, D.J. Wronkiewicz, J. Sproull, W.L. Bourcier, B.P. McGrail, and M.K. Altenhofen (1994). *High Level Waste Borosilicate Glass: A Compendium of Corrosion Characteristics*. DOE/EM-0177. Washington, DC: U.S. Department of Energy Office of Waste Management.

Dick, J.M. (2019). CHNOSZ: Thermodynamic calculations and diagrams for geochemistry. *Frontiers in Earth Science* **7** (180). doi: 10.3389/feart.2019.00180.

Dohmen, L., C. Lenting, R.O.C. Fonseca, T. Nagel, A. Heuser, T. Geisler, and R. Denkler (2013). Pattern Formation in Silicate Glass Corrosion Zones. *International Journal of Applied Glass Science* **4** (4), p. 357–370.

Ebert, W. (2017). DOE High-Level Waste Glass Corrosion Model and Its Implementation in Safety Analysis. Presented to the U.S. Nuclear Waste Technical Review Board at the Summer (2017) Board Meeting, Richland, WA. https://www.nwtrb.gov/docs/default-source/meetings/2017/june/ebert.pdf?sfvrsn=4).

Ebert, W.L. and Jantzen, C.M. (2017) Stage 3 HLW Glass Degradation Model. Presented to the U.S. Nuclear Waste Technical Review Board at the Summer 2017 Board Meeting, Richland, WA. https://www.nwtrb.gov/docs/default-source/meetings/2017/june/talk-7-ebert_jantzen.pdf?sfvrsn=4.

Finch, R. J., and R. C. Ewing (1997). Clarkeite: New Chemical and Structural Data. *American Mineralogist*, *82*, p. 607-619.

Fournier, M., S. Gin, P. Frugier, and S. Mercado-Depierre (2017). Contribution of zeolite-seeded experiments to the understanding of resumption of glass alteration. *npj Materials Degradation* **1**, doi: 10.1038/s41529-017-0018-x.

Fournier, M., S. Gin, P. Frugier, and S. Mercado-Depierre (2018). Application of GRAAL model to the resumption of International Simple Glass alteration. *npj Materials Degradation* **2**, article 21. doi:10.1038/s41529-018-0043-4.

Fournier, M., Gin, S. and Frugier, P. (2014) Resumption of nuclear glass alteration: state of the art. *Journal of Nuclear Materials* **448**, 348-363.

Freeze, G., J.G. Argüello, J. Bouchard, L. Criscenti, R. Dewers, H.C. Edwards, D. Sassani, P.A. Schultz, and Y. Wang (2011). *Nuclear Energy Advanced Modelining and Simulation (NEAMS) Waste Integrated Performance and Safety Codes (IPSC): FY10 Development and Integration.* SAND2011-0845. Albuquerque, NM: Sandia National Laboratories.

Fournier, M., Frugier, P. and Gin, S. (2018) Application of GRAAL model to the resumption of International Simple Glass alteration. npj Materials Degradation 2, 21.

Frugier, P., T. Chave, S. Gin, and J.-E. Lartigue (2009). Application of the GRAAL model to leaching experiments with SON68 nuclear glass in initially pure water. *Journal of Nuclear Materials* **392** (3), p. 552–567.

Frugier, P., S. Gin, Y. Minet, T. Chave, B. Bonin, N. Godon, J.-E. Lartigue, P. Jollivet, A. Ayral, L. De Windt, and G. Santarini (2008). SON68 nuclear glass dissolution kinetics: Current state of knowledge and basis of the new GRAAL model. *Journal of Nuclear Materials* **380** (1–3), p. 8–21.

Gailhanou, H., Blanc, P., Rogez, J., Mikaelian, G., Horiuchi, K., Yamamura, Y., Saito, K., Kawaji, H., Warmont, F. and Grenèche, J.-M. (2013). Thermodynamic properties of saponite, nontronite, and vermiculite derived from calorimetric measurements. *American Mineralogy* **98**, p. 1834-1847.

Gasperin, M. (1986). $Na_2U_2O_7$: Synthese et Structure d'un Monocristal. *Journal of the Less-Common Metals*, **119**, p. 83-90.

Geisler, T., L. Dohmen, C. Lenting, and M.B.K. Fritzsche (2019). Real-time in situ observations of reaction and transport phenomena during silicate glass corrosion by fluid-cell Raman spectroscopy. *Nature Materials* **18**, [p.342–348. doi: 10.1038/s41563-019-0293-8.

Geisler, T., Janssen, A., Scheiter, D., Stephan, T., Berndt, J. and Putnis, A. (2010). Aqueous corrosion of borosilicate glass under acidic conditions: A new corrosion mechanism. *Journal of Non-Crystalline Solids* **356** (28–30), p 1458–1465.

Geisler, T., T. Nagel, M.R. Kilburn, A. Janssen, J.P. Icenhower, R.O.C. Fonseca, M. Grange, and A.A. Nemchin (2015). The mechanism of borosilicate glass corrosion revisited. *Geochimica et Cosmochimica Acta* **158**, p. 112–129.

Giammar, D.E. and Hering, J.G. (2004) Influence of dissolved sodium and cesium on uranyl oxide hydrate solubility. *Environ Sci Technol* **38**, 171-179.

Gin, S. (1995). Control of R7T7 Nuclear Glass Alteration Kinetics Under Saturation Conditions. In Symposium V – Scientific Basis for Nuclear Waste Management XIX, eds. W.M. Murphy and D.A. Knecht, 189–196. Pittsburgh, PA: Materials Research Society.

Gin, S., Jégou, C., Frugier, P. and Minet, Y. (2008) Theoretical consideration on the application of the Aagaard–Helgeson rate law to the dissolution of silicate minerals and glasses. *Chemical Geology* **255**, 14-24.

Gin, S., P. Jollivet, M. Fournier, C. Berthon, Z.Y. Wang, A. Mitroshkov, S.H. Zhu, and J.V. Ryan (2015). The fate of silicon during glass corrosion under alkaline conditions: A mechanistic and kinetic study with the International Simple Glass. *Geochimica et Cosmochimica Acta* **151**, p. 68–85.

Gislason, S.R. and E.H. Oelkers (2003). Mechanism, rates, and consequences of basaltic glass dissolution: II. An experimental study of the dissolution rates of basaltic glass as a function of pH and temperature. *Geochimica et Cosmochimica Acta* **67** (20), p. 3817–3832.

Gorman-Lewis, D., Fein, J.B., Burns, P.C., Szymanowski, J.E.S. and Converse, J. (2008) Solubility measurements of the uranyl oxide hydrate phases metaschoepite, compreignacite, Na–compreignacite, becquerelite, and clarkeite. *Journal of Chemical Thermodynamics* **40**, p. 980-990.

Hamilton, J.P., S.L. Brantley, C.G. Pantano, L.J. Criscenti, and J.D. Kubicki (2001). Dissolution of nepheline, jadeite and albite glasses: Toward better models for aluminosilicate dissolution. *Geochimica et Cosmochimica Acta* **65** (21), p. 3683–3702.

Hamilton, J.P., C.G. Pantano, and S.L. Brantley (2000). Dissolution of albite glass and crystal. *Geochimica et Cosmochimica Acta* **64** (15), p. 2603–2615.

Hellmann, R., S. Cotte, E. Cadel, S. Malladi, L.S. Karlsson, S. Lozano-Perez, M. Cabie, and A. Seyeux (2015). Nanometre-scale evidence for interfacial dissolution-reprecipitation control of silicate glass corrosion. *Nature Materials* **14** (3), p. 307–311.

Ijdo, D. J. W., S. Akerboom, and A.Bontenbal (2015). Crystal Structure of α- and β-$Na_2U_2O_7$: From Rietveld Refinement Using Powder Neutron Diffraction Data. *Journal of Solid State Chemistry*, *221*, 1–4

Ives, D. J. G., Janz, G. J. (1961). *Reference Electrodes: Theory and Practice.* Academic Press, N.Y. 1961.

Jantzen, C.M. and Crawford, C.L. (2015) Hierarchical Modeling of HLW Glass-Gel-Solution Systems for Stage 3 Glass Degradation. MRS Online Proceedings Library (OPL) 1744, 173-184.

Jantzen, C.M., C.L. Trivelpiece, C.L. Crawford, J.M. Pareizs, and J.B. Pickett (2017a). Accelerated Leach Testing of GLASS (ALTGLASS): I. Informatics approach to high level waste glass gel formation and aging. *International Journal of Applied Glass Science* **8** (1), p. 69–83.

Jantzen, C.M., C.L. Trivelpiece, C.L. Crawford, J.M. Pareizs, and J.B. Pickett (2017b). Accelerated Leach Testing of Glass (ALTGLASS): II. Mineralization of hydrogels by leachate strong bases. *International Journal of Applied Glass Science* **8** (1), p. 84–96.

Jollivet, P., Gin, S. and Schumacher, S. (2012) Forward dissolution rate of silicate glasses of nuclear interest in clay-equilibrated groundwater. *Chemical Geology* 330-331, 207-217.

Jové Colón, C. F. and Sassani, D.C. (2021) Waste Forms Inventories, Models, & Testing – Introduction/Overview, SFWD Working Group Meeting (Virtual), May 2021. SAND2021-5964 PE, Sandia National Laboratories, Albuquerque, NM USA.

Linard, Y., Yamashita, I., Atake, T., Rogez, J. and Richet, P. (2001a) Thermochemistry of nuclear waste glasses: an experimental determination. *Journal of Non-Crystalline Solids* **286**, 200-209.

Linard, Y., Advocat, T., Jégou, C. and Richet, P. (2001b) Thermochemistry of nuclear waste glasses: application to weathering studies. *Journal of Non-Crystalline Solids* **289**, 135-143.

McGrail, B.P., W.L. Ebert, A.J. Bakel, and D.K. Peeler (1997). Measurement of kinetic rate law parameters on a Na-Cl-Al borosilicate glass for low-activity waste. *Journal of Nuclear Materials* **249** (2–3), p. 175–189.

McGrail, B.P., J.P. Icenhower, D.K. Shuh, P. Liu, J.G. Darab, D.R. Baer, S. Thevuthasen, V. Shutthanandan, M.H. Engelhard, C.H. Booth, and P. Nachimuthu (2001). The structure of Na_2O-Al_2O_3-SiO_2 glass: impact on sodium ion exchange in H_2O and D_2O. *Journal of Non-Crystalline Solids* **296**, p. 10–26.

Murphy, K.A., N.M. Washton, J.V. Ryan, C.G. Pantano, and K.T. Mueller 2013. Solid-state NMR examination of alteration layers on nuclear waste glasses. *Journal of Non-Crystalline Solids* **369** (June), p. 44–54.

Keller, C. (1975). In: C. Keller (Ed.), Gmelin Handbuch der Anorganischen Chemie, Uran, No.55, Springer Verlag, Berlin.

King, W. D., T. B. Edwards, D. T. Hobbs, and W. R. Wilmarth (2010). Solubility of Uranium and Plutonium in Alkaline Savannah River Site High Level Waste Solutions. *Separation Science and Technology*, **45**, 1793–1800.

Kovba, L. M., Y. P. Simanov, E. A. Ippolitova, and V. J. Spitsyn (1958). An X-ray Study of Alkali Metal Uranates. *Doklady Akademii Nauk SSSR*, **120**, 1042-1044.

Kovba, L. M. (1972). *Sov. Radiochem. Engl. Trans.*, **14**, 746.

Kresse, G., and J. Furthmüller (1996). Efficient iterative schemes for ab initio total-energy calculations using a plane-wave basis set. *Physical Review B,* **54**(16), 11169–11186.

Mariner, P. E., Connolly, L. A., Cunningham, L. J., Debusschere, B. J., Dobson, D. C., Frederick, J. M., Wallace, M. G. (2019). Progress in Deep Geologic Disposal Safety Assessment in the U.S. since 2010. Sandia National Laboratories. SAND2019-12001R.

Metz, V., Loida, A., Bohnert, E., Schild, D. and Dardenne, K. (2008) Effects of hydrogen and bromide on the corrosion of spent nuclear fuel and γ-irradiated UO2 (s) in NaCl brine. *Radiochim Acta* **96**, 637-648.

Moffat, H.K. and Jové Colón, C.F. (2009) Implementation of Equilibrium Aqueous Speciation and Solubility (EQ3 type) Calculations into Cantera for Electrolyte Solutions, SAND2009-3115. Sandia National Laboratories, Albuquerque, N.M., p. 146.

Moffat, H.K. and Jové Colón, C.F. (2021) 0D Modeling of Reactor Networks Within Zuzax, SAND2021-10765. Sandia National Laboratories, Albuquerque, N.M.

Moog, H. C., F. Bok, C.M. Marquardt, V. Brendler (2015). Disposal of nuclear waste in host rock formations featuring high-saline solutions – Implementation of a thermodynamic reference database (THEREDA). Applied Geochemistry 55 (2015), p. 72–84.

Muller, I.S., Ribet, S., Pegg, I.L., Gin, S. and Frugier, P. (2006) Characterization of alteration phases on HLW glasses after 15 years of PCT leaching. Ceramic transactions 176, 191.

Neeway, J.J., Parruzot, B.P., Bonnett, J.F., Reiser, J.T., Kerisit, S.N., Ryan, J.V. and Crum, J.V. (2020) Acceleration of glass alteration rates induced by zeolite seeds at controlled pH. *Applied Geochemistry* **113**, 104515.

Oelkers, E.H. and S.R. Gislason (2001). The mechanism, rates and consequences of basaltic glass dissolution: I. An experimental study of the dissolution rates of basaltic glass as a function of aqueous Al, Si and oxalic acid concentration at 25°C and pH=3 and 11. *Geochimica et Cosmochimica Acta* **65** (21), p. 3671–3681.

Parkhurst, D. L. (1995). User's guide to PHREEQC, a computer program for speciation, reaction-path, advective-transport, and inverse geochemical calculations. U.S. Geological Survey; U.S. Geological Survey, Earth Science Information Center, Open-File Reports Section, Water-Resources Investigations Report 95-4227, viii, 143 p.

Perdew, J., J. Chevary, S. Vosko, K. Jackson, M. Pederson, D. Singh, et al. (1992). Atoms, Molecules, Solids, and Surfaces - Applications of the Generalized Gradient Approximation for Exchange and Correlation. *Physical Review B, 46*(11), 6671–6687.

Perdew, J. P., K. Burke, and M. Ernzerhof (1996). Generalized gradient approximation made simple. *Physical Review Letters, 77*, 3865.

Pierce, E.M., L.R. Reed, W.J. Shaw, B.P. McGrail, J.P. Icenhower, C.F. Windisch, E.A. Cordova, and J. Broady, J. (2010). Experimental determination of the effect of the ratio of B/Al on glass dissolution along the nepheline ($NaAlSiO_4$)-malinkoite ($NaBSiO_4$) join. *Geochimica et Cosmochimica Acta* **74** (9), p. 2634–2654.

Pierce, E.M., Rodriguez, E.A., Calligan, L.J., Shaw, W.J. and Pete McGrail, B. (2008) An experimental study of the dissolution rates of simulated aluminoborosilicate waste glasses as a function of pH and temperature under dilute conditions. *Applied Geochemistry* 23, 2559-2573.

Putnis, A. (2015). Glass corrosion: Sharpened interface. *Nature Materials* **14** (3), p.261–262.

Ragoussi, M.-E., D. Costa, 2019. Fundamentals of the NEA Thermochemical Database and its influence over national nuclear programs on the performance assessment of deep geological repositories. *Journal of Environmental Radioactivity* **196** (2019), p. 225-231.

Ribet, S., Muller, I.S., Pegg, I.L., Gin, S. and Frugier, P. (2004) Compositional Effects on the Long-Term Durability of Nuclear Waste Glasses: A Statistical Approach. MRS Online Proceedings Library 824, 240-245.

Ryan, J.V., Parruzot, B., Lines, A.M., Bryan, S.A., Seymour, L.M., Bonnett, J.F. and Motkuri, R.K. (2019) In-situ monitoring of seeded and unseeded stage III corrosion using Raman spectroscopy. npj Materials Degradation 3, 1-7.

Saine, M.-C. (1989). Synthèse et Structure de $K_2[(UO_2)_2O_3]$ Monoclinique. J. Less-Common Met., 154, 361−365.

Sassani, D., L. Price, R. Rechard, R. Rogers, W. Walkow, A. Johnson, A. Sanchez, P. Mariner, M. Rigali, E. Stein, and P. Weck (2017). Inventory and Waste Characterization Status Report. SFWD-SFWST-2017-000014; SAND-2017-10260 R. Albuquerque, NM: Sandia National Laboratories.

Smith, A. L., P. E. Raison, and R. J. M. Konings (2011). Synthesis and Crystal Structure Characterisation of Sodium Neptunate Compounds. *Journal of Nuclear Materials*, *413*, 114−121.

Smith, A. L., P. E. Raison, L. Martel, T. Charpentier, I. Farnan, D. Prieur, C. Hennig, A. C. Scheinost, R. J. M. Konings, and A. K. Cheetham (2014). A ^{23}Na Magic Angle Spinning Nuclear Magnetic Resonance, XANES, and High-Temperature X-ray Diffraction Study of $NaUO_3$, Na_4UO_5, and $Na_2U_2O_7$. *Inorg. Chem.*, **53**, 375−382.

Smith, A.L., C. Gueneau, J.-L. Fleche, S. Chatain, O. Benes, R.J.M. Konings (2017). Thermodynamic assessment of the Na-O and Na-U-O systems: Margin to the safe operation of SFRs. *Journal of Chemical Thermodynamics* **114**, 93–115

Strachan, D. (2017) Glass dissolution as a function of pH and its implications for understanding mechanisms and future experiments. *Geochimica et Cosmochimica Acta* **219**, 111-123.

Strachan, D.M. and J.J. Neeway 2014. Effects of alteration product precipitation on glass dissolution. *Applied Geochemistry* **45**, p.144–157.

Strachan, D.M. (2001) Glass dissolution: testing and modeling for long-term behavior. *Journal of Nuclear Materials* **298**, 69-77.

Strachan, D.M. and Croak, T.L. (2000) Compositional effects on long-term dissolution of borosilicate glass. *J Non-Cryst Solids* 272, 22-33.

Togo, A., F. Oba, and I. Tanaka (2008). “First-principles calculations of the ferroelastic transition between rutile-type and CaCl2-type SiO2 at high pressures” *Phys. Rev.* B, *78*, 134106.

Van Iseghem, P. and Grambow, B. (1987) The long-term corrosion and modelling of two simulated Belgian reference high-level waste glasses. MRS Online Proceedings Library Archive 112.

Vienna, J.D., Neeway, J.J., Ryan, J.V. and Kerisit, S.N. (2018) Impacts of glass composition, pH, and temperature on glass forward dissolution rate. npj Materials Degradation 2, 22.

Vienna, J.D., Ryan, J.V., Gin, S. and Inagaki, Y. (2013) Current understanding and remaining challenges in modeling long-term degradation of borosilicate nuclear waste glasses. International *Journal of Applied Glass Science* **4**, 283-294.

Vinet, P., J. R. Rose, J. Ferrante, and J. R. Smith (1989). Universal features of the equation of state of solids. *J. Phys.: Condens. Matter*, *1*, 1941.

Weck, P. F., E. Kim, C. F. Jové-Colón, and D. C. Sassani (2012). Structures of uranyl peroxide hydrates: a first-principles study of studtite and metastudtite. *Dalton Transactions, 41*(32), 9748–9752.

Weck, P., Brady, P.V., Criscenti, L.J., Fluke, N., Gelbard, F., Padilla, M., Price, L., Prouty, J., Rechard, R., Rigali, M.J., Rogers, R., Sanchez, A., Sassani, D.C., Tillman, J. and Walkow, W. (2021) Annual Status Update for OWL and Waste Form Characteristics (SAND2021-0994 R), Prepared for U.S. DOE Spent Fuel and Waste Science and Technology (M2SF-21SN010309012). Sandia National Laboratories, Albuquerque, NM, 218 pp.

Wolery, T.J. and Jarek, R.L. (2003) EQ3/6, Version 8.0: Software User's Manual. Sandia National Laboratories, Albuquerque, p. 376 pp.

Zhen-Wu, B.Y., Prentice, D.P., Ryan, J.V., Ellison, K., Bauchy, M. and Sant, G. (2020) zeo19: A thermodynamic database for assessing zeolite stability during the corrosion of nuclear waste immobilization glasses. npj Materials Degradation 4, 1-12.